FAKULTÄT FÜR PHYSIK
Institut für Experimentelle Teilchenphysik

Evaluation of the radiation hardness of HitPix3 MAPS

(Bestimmung der Strahlenhärte von HitPix3 MAPS)

Bachelor's thesis
by

Oskar Moritz

Reviewer:	Prof. Dr. U. Husemann
Second Reviewer:	Dr. A. Dierlamm
Advisor:	Bogdan Topko

08.01.2024 – 07.05.2024

ETP-Bachelor-KA/2024-03

Erklärung zur Selbstständigkeit

Ich versichere, dass ich diese Arbeit selbstständig verfasst habe und keine anderen als die angegebenen Quellen und Hilfsmittel benutzt habe, die wörtlich oder inhaltlich übernommenen Stellen als solche kenntlich gemacht und die Satzung des KIT zur Sicherung guter wissenschaftlicher Praxis in der gültigen Fassung vom 24.05.2018 beachtet habe.

Karlsruhe, den 07.05.2024, _____

Oskar Moritz

Contents

List of Figures

List of Tables

1. Introduction

Radiation therapy is widely used as a treatment for cancer patients. As the irradiation with photons strongly damages healthy tissue as well, ion beam therapy can be used to treat tumors surrounded by sensitive organs. In this bachelor's thesis, a new type of particle detector as a beam monitor for ion beam therapy of cancer patients in facilities such as the Heidelberger Ionenstrahl-Therapiezentrum (HIT) is further examined. The HitPix3 detectors are monolithic active pixel sensors (MAPS), combining sensitive volume and signal processing. The HitPix sensors are made of silicon and are divided into pixels, which consist of a diode to detect particles and readout electronics to digitize the signal. As the radiation due to the ion beam can cause damage to the detectors, this thesis aims to evaluate the effect of the damage caused by the ion beam on the monitoring ability of the sensors.

In this chapter, the underlying concepts of ion beam therapy as well as the application at the Heidelberger Ionenstrahl-Therapiezentrum (HIT) are introduced. in chapter 3, the HitPix3 sensor which is examined in this thesis is explained. The measurements, that were conducted are explained in chapter 4. The data gathered from this is then analyzed in chapter 5. The results of the thesis are then summarized in 6.

1.1. Principles of ion beam therapy

The underlying principle of ion beam therapy is the Bragg peak. This describes a sharp peak in the energy deposition of a heavy ion at a certain penetration depth in matter. When charged particles enter into matter such as human tissue, they will interact with it according to a stochastic principle. On average, the first interaction will be made after the particle travels the mean free path corresponding to its velocity. After the interaction, this velocity will decrease, which will increase the probability of another interaction. The mean free path thus decreases. This leads to an exponential increase in the energy deposition over the traveled distance. After a certain distance, the particle will have deposited all of its initial energy into the matter and will stop. After that point, the energy deposition will be zero. The energy deposition of a particle in matter over distance is shown in figure 1.1. The sketch shows the possibility of creating an even energy deposition across the tumor while depositing almost no dose to the tissue behind the tumor and a significantly lower dose to the tissue in front of the tumor compared to the dose deposited in the tumor. This can be achieved by using ions at different energies with different positions and applied doses. Comparing this to the more widely used photons with a wider peak at much lower depths, the dose the healthy tissue receives can be drastically lowered with ion beam therapy.

William Henry Bragg discovered the effect named after him in alpha particles in 1904 but the potential of this discovery for medical purposes was only exploited decades later according to [2]. Ideally, only the tumor and not the healthy tissue is subjected to damage caused by radiation. As there is still some energy deposition between the entry of the particle and the Bragg-peak, some healthy tissue will still experience radiation damage

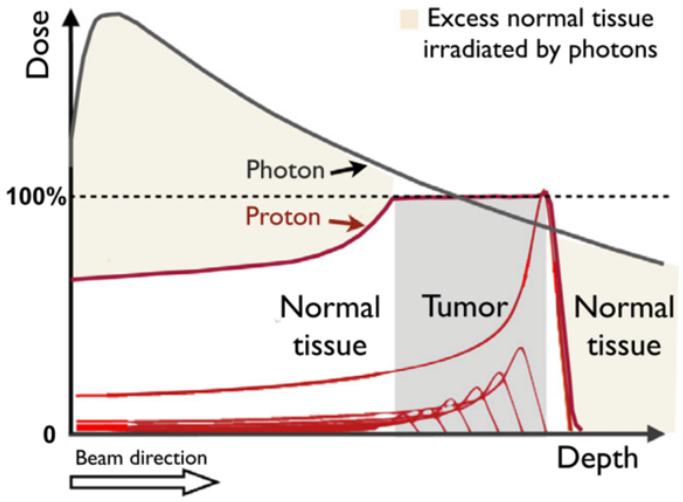

Figure 1.1.: Bragg-peak compared to the energy deposition of photons. Taken from [1]

however much less compared to treatment with gamma rays. An example of a radiation plan both with photons and protons is shown in figure 1.2. The dose, that the healthy tissue receives is shown to be significantly reduced when using protons.

1.2. Heidelberger Ionenstrahl-Therapiezentrum (HIT)

The concept of ion beam therapy has been around for many years now. The potential of the Bragg peak for medical purposes was discovered at the Lawrence Berkeley Laboratory [3]. At the university hospital in Heidelberg, an ion beam therapy treatment center (HIT) was commissioned in 2009 and is now treating 700 patients each year. Currently, both hydrogen ions (protons) and carbon ions are used for treatment. An overview is shown in figure 1.3. The ions produced from hydrogen and carbon in the gaseous phase (1) first get accelerated in a linear accelerator (2) before entering the synchrotron (3) with a diameter of about 20 m and then get distributed (4) to three treatment rooms (5) from which one is equipped with a gantry (8), which allows for irradiation from a wide range of angles [4]. The acceleration reaches the intensities and energies found in table 1.1.

Table 1.1.: Parameters of ion acceleration at HIT. Specifications of the accelerated ions for clinical usage [6]

Ion	Energy in $\frac{\text{MeV}}{\text{u}}$	Intensity in s^{-1}
Hydrogen (Proton)	48 – 221	1.2×10^8 – 3.2×10^9
Carbon	88 – 430	5×10^6 – 8×10^7

Currently, multi-wire chambers are utilized to monitor the position and width of the beam at HIT. The intensity is measured using an ionization chamber. In the future, the beam monitoring system needs to cope with the simultaneous use of MRI, which negatively influences multi-wire chambers due to both strong changing electromagnetic fields and mechanical vibrations. Multi-wire chambers also pose the problem of inhomogeneous material distribution with strong scattering at the wires. The HitPix sensors are supposed to solve both problems while being able to measure the intensity, position and width of the beam.

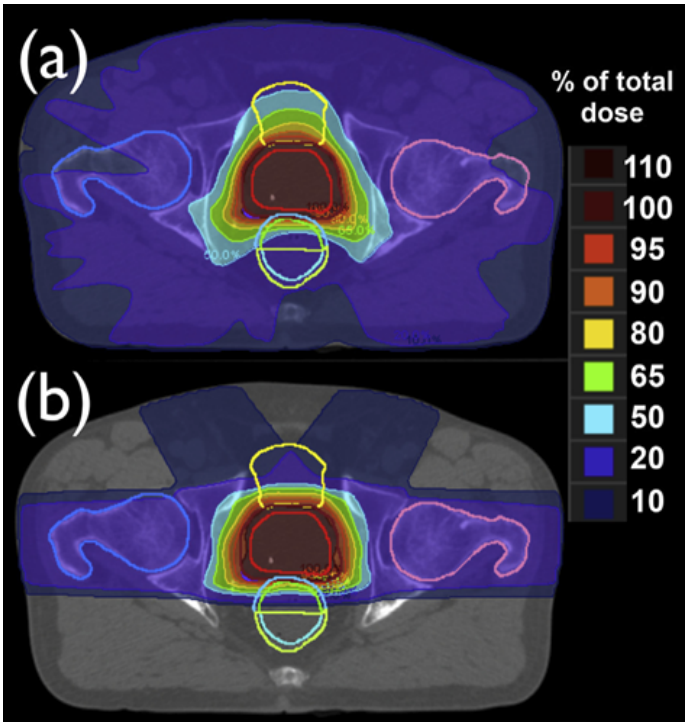

Figure 1.2.: Example of a radiation plan with photons and protons (a) shows a plan for the irradiation with photons and (b) for protons. The colors indicate the radiation dose compared to the dose the tumor receives. The treatment plans are shown for the same cross-section image of the pelvis. Body parts are outlined in red (prostate), yellow (bladder), pink and dark blue (bones) light blue and green (rectum) Taken from [1]

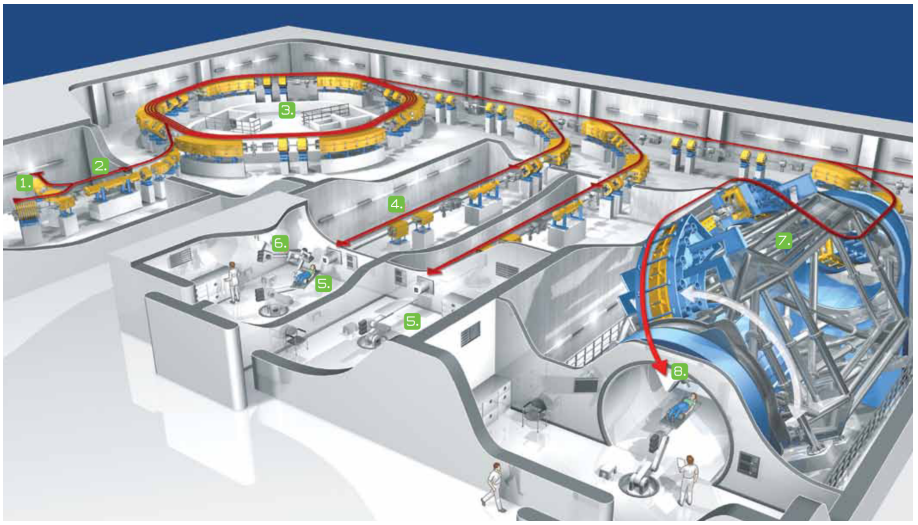

Figure 1.3.: Sketch of the layout of HIT including ion sources, linear accelerator, synchrotron, distribution to treatment rooms and gantry. Taken from [5]

2. Physics Background

2.1. Silicon detectors

In principle, silicon detectors work like operating a semiconductor diode consisting of a pn-junction in reverse bias (negative potential connected to p-type) to create a wide depletion layer. When ionizing radiation passes through this depletion layer, electron-hole pairs can be created, which move to the electrodes in the detector. This creates a current, which generates an analog signal in a charge sensitve amplifier. The analog signal is then further processed. The depth of the depletion zone d depends on the bias voltage U roughly according to

$$d \propto \sqrt{|U|}. \tag{2.1}$$

As a larger volume of the depletion zone allows for a longer path length in the sensitive volume, more electron-hole pairs are created leading to a stronger analog signal. This allows for easier distinguishing between signal and noise.

2.2. Leakage current of diodes

A diode operated in reverse bias shows a low but non-zero leakage current. It is shown in figure 2.1. Before the breakdown voltage is reached, the leakage current is proportional to the square root of the reverse bias voltage.

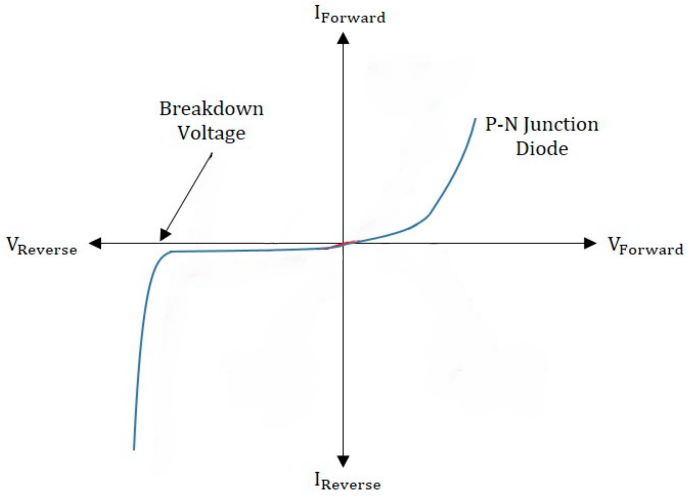

Figure 2.1.: Leakage current of a pn-junction. Shown is the expected leakage current depending on the bias voltage. Adapted from [7]

In this thesis, the leakage current is relevant not only because it can be used to detect broken sensors but also because the leakage current is an indicator of radiation-induced damage. According to [8], the leakage current per depleted volume $\frac{I}{V}$ is proportional to the fluence Φ of particles causing non-ionizing energy loss the sensor received. Equation 2.2 shows this dependency.

$$\frac{I}{V} = \nu \cdot \Phi \tag{2.2}$$

As temperature dependent measurements are performed in this thesis, the temperature dependence of the leakage current will be analyzed. According to [9], the following applies to the leakage current I:

$$I \propto T^2 \cdot \mathrm{e}^{-\frac{1.21\,\mathrm{eV}}{2k_\mathrm{B}T}}, \tag{2.3}$$

where T is the absolute temperature and k_B is the Boltzmann constant.

2.3. Signal generation

The beam monitor, which will eventually be used at the irradiation facility will measure ions with high ionizing power. These highly ionizing particles (HIPs) cannot be used for practical reasons during most of the testing of the sensors in the course of this thesis. Instead, minimally ionizing particles (MIPs) are used, in this case, beta particles from a Sr-90 source. A MIP is a particle that has an energy leading to a minimum of the stopping power in a certain material. An example of how the stopping power depends on the particle momentum is shown in figure 2.2.

The successful detection of MIPs ensures the detection of HIPs as the signal generated in the detector is always higher. The measured efficiencies of the irradiated sensors thus represent a lower limit for the final detector. Because of this, Sr-90 is used to test the sensor in this thesis.

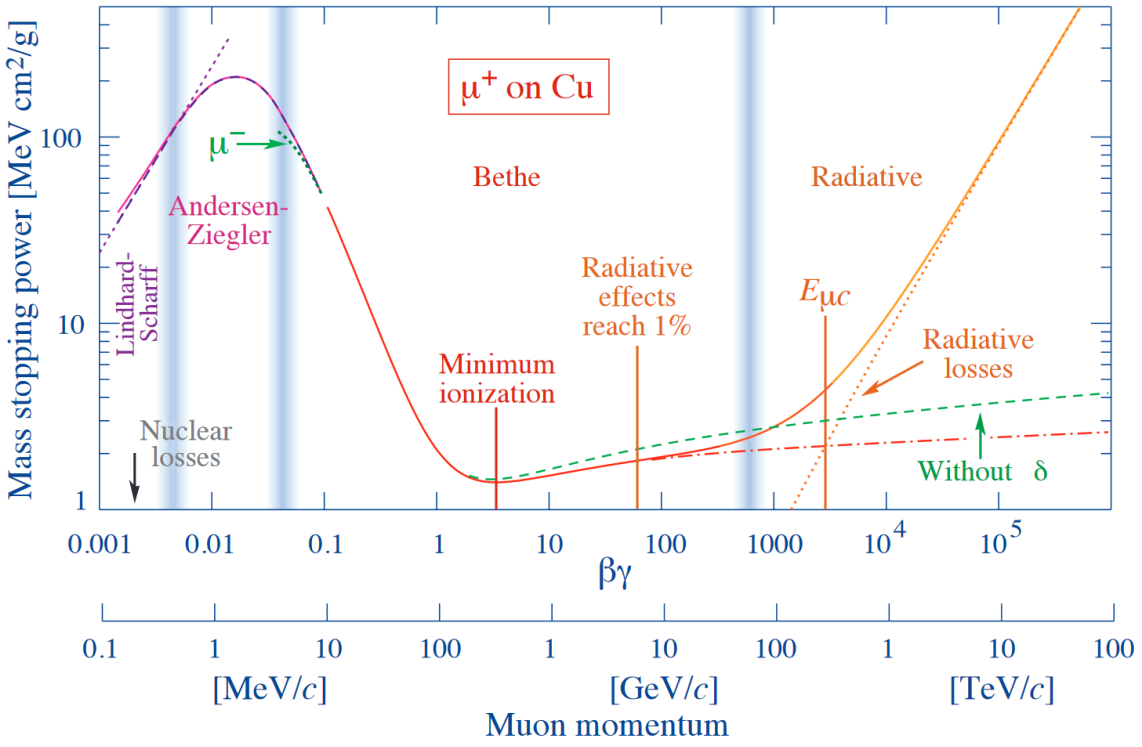

Figure 2.2.: Stopping power as a function of momentum at the example of copper and an anti-muon. The plot shows the energy loss of an anti-muon in copper depending on its momentum. Taken from [10] (page 551)

3. Design and working principle of HitPix3

The HitPix3 Sensor is the third iteration of a sensor based on HV-CMOS technology for ion beam therapy as it is done at HIT. In this chapter, the components of the sensor and their function are explained.

3.1. Sensor layout

The HitPix3 sensor is a pixelated silicon sensor built in a high voltage capable complementary metal oxide semiconductor (HV-CMOS) fabrication process. The detecting part of the sensor consists of a pn-junction which is operated in reverse bias with voltages above 100 V. Each pixel features additional amplifying and digitizing electronics. The sensor is designed with the readout electronics above the detecting diode. A schematic of the realization is shown in figure 3.1. The layout of one pixel shows the grid of high voltage connections to the substrate to enable an evenly wide depletion zone. The HitPix3 sensor consists of 48 × 48 pixels with a size of 200 µm × 200 µm. The final sensor layout will be twice as big consisting of 96 × 96 pixels. These sensors are then used to build a 13 × 13 matrix covering the required area of 25 cm × 25 cm.

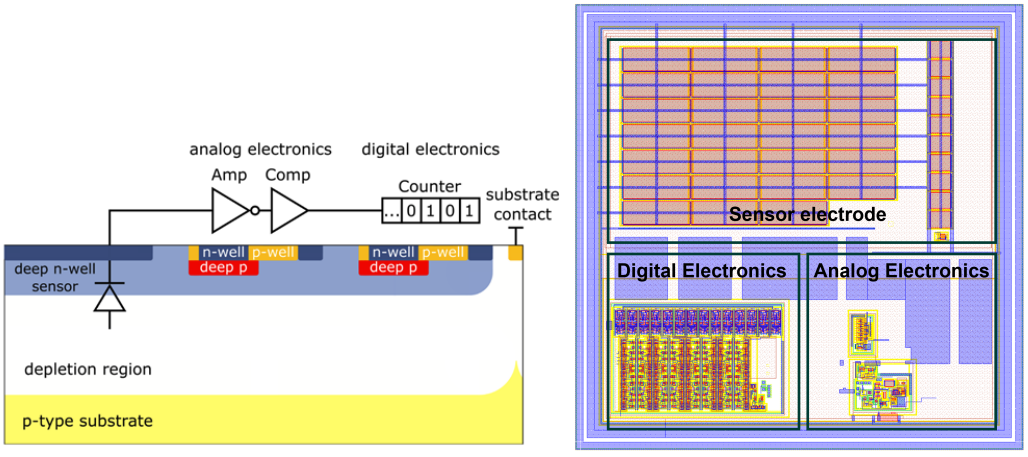

Figure 3.1.: Sensor structure of one HitPix3 pixel with common n-well Simplified pixel cross-section (left) and layout (right). Taken from [6]

3.2. In-pixel readout electronics

Figure 3.1 also shows the position of the in-pixel electronics located above the depletion region. These consist of an analog and a digital part. The in-pixel electronics allow the sensor to be much more easily connected to its data-processing environment as otherwise, each pixel would need an individual connection. A simple schematic of the in-pixel readout

electronics is shown in figure 3.2. It shows the charge sensitive amplifier that is used to convert and amplify the induced charge from the diode into an analog signal before it is digitized in the comparator and fed to an in-pixel counter from where it can be read out. Not shown in the schematic is the dac-tune setup. The comparator receives a global threshold voltage, created in a digital-analog converter (DAC) located in the peripheral electronics part of the sensor from an 8-bit global threshold setting, and the dac-tune voltage of each pixel. This dac-tune voltage is created in an in-pixel DAC from a 4-bit value written in a random access memory (RAM) cell in the pixel. The digital dac-tune value is loaded into the RAM using the sensor's peripheral electronics.

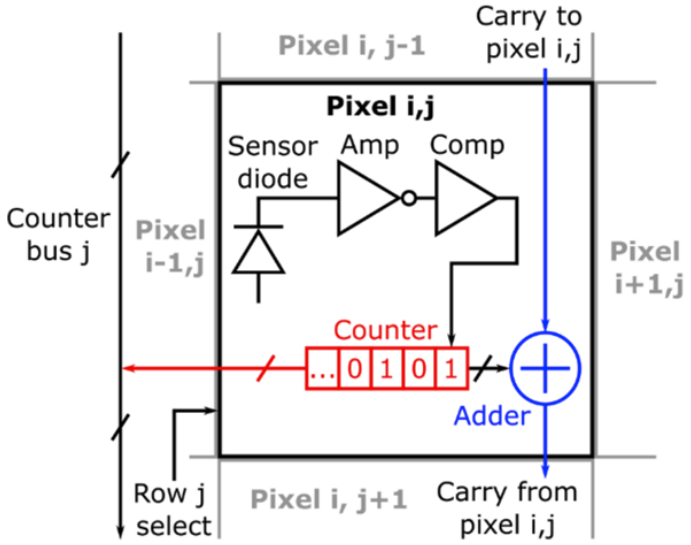

Figure 3.2.: Simplified schematic of the HitPix in-pixel readout electronics. Taken from [6]

3.3. Readout modes

As previously discussed, the in-pixel electronics create a digital signal which is used to increment the number of recorded hits. This number can be read out by two readout modes:

- Counter readout mode
- Adder readout mode

The sensor has a shift register, which is used for the readout. When using the counter readout mode, the shift register is used to load the hit counts of the pixels row per row into the register and push them out to the connected external readout electronics. When using the adder readout mode, each pixel adds its own hit count to the count received from the previous pixel before transferring the value to the next pixel. A schematic of this process is shown in figure 3.3. The resulting sums from each column are then loaded into the shift register, from where they are read out. This is done both column-wise and row-wise. The resulting sums can be used to create a profile of the beam allowing the construction of the required information for the beam monitoring. As this is much faster than the counter readout mode, this will be used in the final system. For testing and debugging, the counter mode can be used as it allows the readout of individual pixels. Both of these readout modes are frame-based. This means the number of detections is summed up for a predefined time (the frame time) and then read out.

Important parameters for the operation of the shift register are the frequency at which the data from the shift register is read out and the delay between the signal, that triggers the data transfer and the sampling of the data.

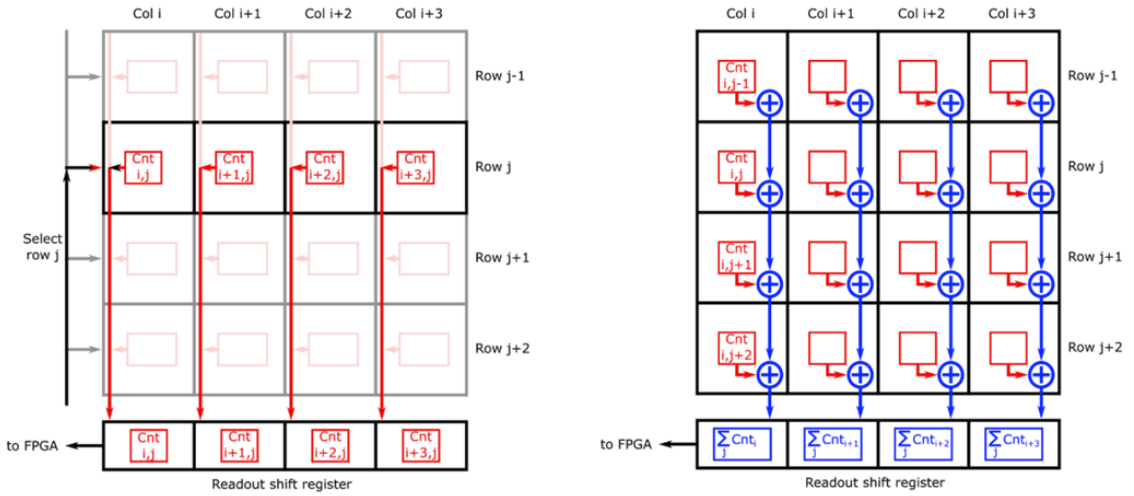

Figure 3.3.: Schematic of the readout modes. Counter readout mode (left) and adder readout mode (right). Taken from [6]

3.4. Data acquisition system

To use the sensors, a data acquisition system is needed, which can supply the sensor with the necessary electric power, configure the sensor and process the recorded data into a format which can be read out by a PC.

The connection of the PC to the sensor is done in several steps, which are presented in figure 3.4. The sensor itself is glued to a carrier printed circuit board (PCB). The connection to the PCB is made with wire bonds. The carrier PCB is connected via a PCIe connector to the generic configuration and control (GECCO) board. The GECCO board is connected to external power supplies and distributes the power to the carrier PCB. It is also used to generate test signals used during the characterization process as well as to transfer configuration and readout data between the carrier PCB and the field programmable gate array (FPGA). The FPGA is connected to a PC via a USB interface and is running the firmware for the sensor.

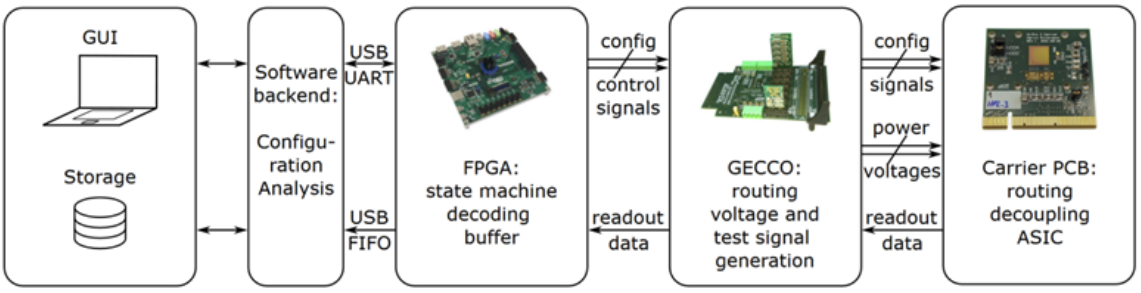

Figure 3.4.: Schematic of the external readout electronics. Taken from [6]

As previously mentioned, the GECCO board connects external power sources to the carrier PCB and thus the sensor. This includes the high-voltage power supply, which is used to deplete the diode. During the measurements done for this thesis, voltages up to $U_{\text{bias}} = -150\,\text{V}$ were used. Additionally, low-voltage power is needed:

- Analog in-pixel electronics requires $V_{\text{SSA}} = 1.25\,\text{V}$ and $V_{\text{DDA}} = 1.85\,\text{V}$.
- Power for digital electronics $V_{\text{DDD}} = 1.95\,\text{V}$
- Operating voltage of the GECCO board $V_{\text{G}} = 3.33\,\text{V}$

4. Experimental Investigations

In this chapter, the measurements conducted in this thesis will be discussed. This includes explanations of the measurements that are taken as well as the practical process with the challenges this poses.

4.1. Measurement procedure

As the goal of this thesis is the evaluation of the radiation hardness of the HitPix3 sensors, a system needs to be found that allows to rate the performance of the detectors after radiation. This should reveal whether the sensor is still working in principle and how well it is able to locate the particle beam. The results should also include any temperature dependencies.

For the first part, the basic characteristics of the components of the sensor will be measured. This includes the leakage current depending on the reverse bias voltage. This provides information about the extent of the damage to the sensor bulk. Next, the readout electronics are examined. A latency scan is done to ensure the peripheral electronics are working as expected. In order to test the in-pixel readout electronics, an artificial signal with various amounts of charge is created on the GECCO board, fed to the comparator and the resulting digital signal is recorded. This procedure is called charge injection measurement.

As testing of the sensors in the actual particle beam at HIT is not possible to the extent it would be needed for this study, the beam will be simulated with a Sr-90 source which, as discussed in section 2.3, provides minimum ionizing particle.

To determine how well the sensors can locate the particle beam, a Sr-90 source is placed on top of the sensors and frames are recorded for both readout modes and with various reverse bias, global threshold settings and temperatures. Additionally, the noise is recorded without the source for the same settings. It can then be evaluated how well the position of the source is visible and which settings need to be chosen for optimal results. From these results, the ideal operation parameters can be determined.

In the following paragraphs, the above-mentioned measurements are explained further.

4.1.1. Leakage current measurement

As the leakage current is an indicator of the damage to the sensor bulk caused by the irradiation, it is important to measure it. This is done by applying different high voltages via the external power supply, waiting 5 s for the current to adjust and then recording the drawn current 15 times. The measured value is the average of this.

4.1.2. Latency scan

During the latency scan, random data is loaded into the shift register and read out at different frequencies. Additionally to these varied readout rates, the sampling latency is

varied. This is the delay between the signal to read out the shift register and the sampling of the data. The read data is then compared to the data that was loaded in to obtain the number of readout errors. To ensure the shift register can operate at a certain frequency, there has to exist a window of sampling latencies for which the number of errors is zero.

4.1.3. Charge injection measurement

The charge injection measurement aims to test the in-pixel readout electronics. On the GECCO board, small charge pulses of varying amplitude are generated and fed to the in-pixel electronics. The pulses are generated by loading a capacitor with a varying voltage and unloading it through the charge sensitive amplifier. For each voltage, several pulses are injected. The number of injections can then be compared to the number of hits each pixel detects. This is done for several global threshold settings.

This kind of measurement is also used to perform the dac-tune optimization. The pixel's dac-tune setting is adjusted to create a uniform response to the charge injection measurement for all global threshold settings.

The charge injection measurement can be done with and without a previous dac-tune optimization. The comparison can be used to rate the optimization.

4.1.4. Frame measurement

During a frame measurement, multiple frames are recorded. For each frame the pixels record and count detections for a fixed frame length of 5 ms. After each frame, the accumulated counts are read out depending on the readout mode. The average detection rate can then be calculated as the sum of the detections of all frames divided by the frame length times the number of frames. The frame measurement can be recorded with both readout modes.

4.2. Measurements taken

The available sensors can be divided into four unirradiated ones from which one was used during a beam test at HIT resulting in slight radiation damage and five irradiated ones. The irradiated detectors were uniformly irradiated at KAZ with a dose that produces damage comparable to what the center of the detector will receive after approximately one year of use at the ion beam therapy facility. This is explained in detail in section 4.3. All sensors were diced from the same wafer (number 4). They are then enumerated from 6 to 10 for the irradiated ones and 11 to 14 for the unirradiated ones.

Before temperature dependent measurements are taken in the climatic chamber, all sensors are measured at room temperature ($\approx 22\,^{\circ}\mathrm{C}$). They all undergo a full characterization, consisting of an IV measurement with the low-voltage power supply turned off. The low-voltage power supply powers the in-pixel electronics, which are not needed for the measurement of the leakage current. Then, a latency scan, a charge injection measurement and frame measurements with both readout modes are performed. The latter two are done with and without dac-tune optimization before.

Except for sensor number 9, all sensors have undergone at least one full temperature dependent characterization. A full characterization is done at different temperatures. Those are $20\,^{\circ}\mathrm{C}$, $10\,^{\circ}\mathrm{C}$, $5\,^{\circ}\mathrm{C}$, $0\,^{\circ}\mathrm{C}$, $-10\,^{\circ}\mathrm{C}$ and $-20\,^{\circ}\mathrm{C}$. At each temperature, the sensor is measured. Contrary to the full characterization at room temperature, a latency scan is not recorded. This is due to the fact that the measured sensors all showed the expected performance and this is not suspected to change with varying temperature. Thus, a full temperature dependent characterization consists of:

- IV curve from $0\,\mathrm{V}$ to $-150\,\mathrm{V}$ in steps of $-2\,\mathrm{V}$

- Dac-tune optimization
- Charge injection measurement with thresholds from 140 to 190 in steps of 2
- Frame measurements with both readout modes, with and without a Sr-90 source for different bias voltages from $-30\,\mathrm{V}$ to $-150\,\mathrm{V}$ in steps of $-24\,\mathrm{V}$ and different global threshold settings from 140 to 190 in steps of 2

The full temperature dependent characterization is started at $20\,^{\circ}\mathrm{C}$. Before the measurement at a given temperature is started, there is a waiting time of 5 min after the air temperature in the climatic chamber has reached the set temperature. This is done to ensure the sensors temperature has adapted to the new temperature. The measurements are then done for every temperature down to $-20\,^{\circ}\mathrm{C}$. Then the chamber is heated up again and there is again a waiting time to ensure all electric components in the climatic chamber have heated up to room temperature before opening the chamber to avoid condensation on sensitive components.

4.3. Irradiation at KAZ

The irradiated sensors were irradiated at the Karlsruher Kompaktzyklotron (KAZ), which is operated by the Zyklotron AG [11]. The KAZ is a cyclotron that delivers protons for the irradiation of the sensors. As the beam is not uniform, the target is moved to scan the area in order to receive a uniform irradiation. The sample is cooled with nitrogen gas below $-30\,^{\circ}\mathrm{C}$ to avoid annealing of radiation damage through thermal effects (see [8]). Additionally to the sample, a small piece of nickel foil is irradiated in the same way. The activity of the nickel isotope Ni-57 is used as a measure of the applied proton fluence. In the case of the irradiated sensors used here, this results in a 1 MeV neutron equivalent fluence of $1 \times 10^{15}\,\mathrm{cm}^{-2}$.

5. Discussion of the results

5.1. IV curves

In the following sections, the recorded leakage currents of the HitPix3 sensors depending on the reverse bias voltage are presented. As the leakage current is a measure of radiation damage, these results are especially important to classify the irradiated sensors.

5.1.1. Unirradiated sensors

For reference, the leakage current of the unirradiated sensors is measured as well. For all recorded temperatures, the leakage current with the low voltage power supply turned on is shown in figure 5.1. As it can be seen, the leakage current is extremely low. As the high-voltage power supply has significant uncertainties on the measured current for such low currents, the relative uncertainty is also significant. This also means that uncertainties on the voltage measurement can be neglected. As the sensors are developed for high voltages, it is not expected that the breakdown voltage is reached during the measurements. Thus the leakage current I is expected to depend on the reverse bias voltage U according to equation 5.1.

$$I = a \cdot \sqrt{-U} \tag{5.1}$$

The leakage current of the unirradiated sensors number 12 to 14 is fitted according to equation 5.1 and shown in figure 5.1. All fit parameters can be found in the appendix in table A.1. As the high relative uncertainty on the current suggests, the data points are scattered around the square root fit. Especially between a reverse bias voltage of 0 V to -10 V, the relative uncertainty is very high leading to strong scattering in the recorded data points.

Even though the leakage current of the three sensors differs by more than a factor of two, they all seem to follow the relation in equation 5.1.

As the leakage current was measured at different temperatures, the temperature dependence of the leakage current shall be analyzed. As discussed in 2.2, the leakage current is expected to behave according to:

$$I = \kappa \cdot T^2 \cdot \mathrm{e}^{-\frac{1.21\,\mathrm{eV}}{2k_\mathrm{B}T}} \tag{5.2}$$

The function in equation 5.2 is fitted to the measured leakage currents at a bias voltage of -150 V in figure 5.2. This voltage is chosen as following measurements are made at this voltage to ensure a depletion depth which is as high as possible. Above $T = 0\,^\circ\mathrm{C}$, the data

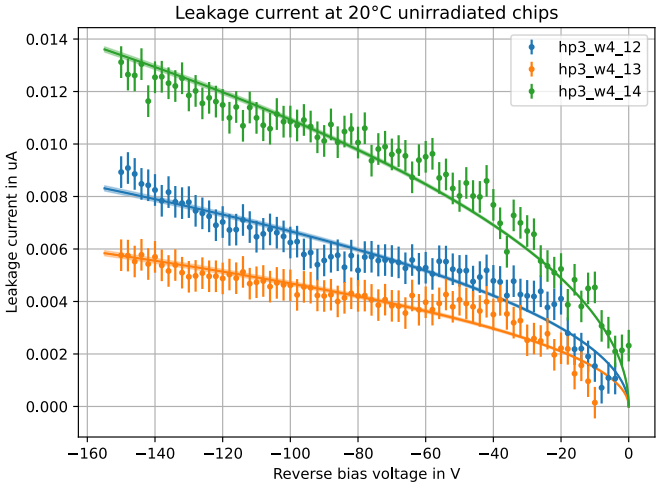

Figure 5.1.: Leakage current of the unirradiated sensors 12,13,14 depending on the reverse bias voltage at $T = 20\,°\mathrm{C}$. The filled area displays the 1σ interval of the fit.

is represented well by the fit. For lower temperatures, this is not the case. Considering the very small current and the relatively high uncertainty of the measurement device, this might be a measurement error. At the measurement range of 1 µA used here, the Keithley 2410 device has an uncertainty of $0.035\,\% + 600\,\mathrm{pA}$. This uncertainty is shown in the error bars in figures 5.1 and 5.2. The relative part of the uncertainty which is 0.035 % of the measured value is very small but the absolute part of the uncertainty of 600 pA is in the same order of magnitude as the measurements at low temperatures. The unirradiated sensors are thus considered working as expected.

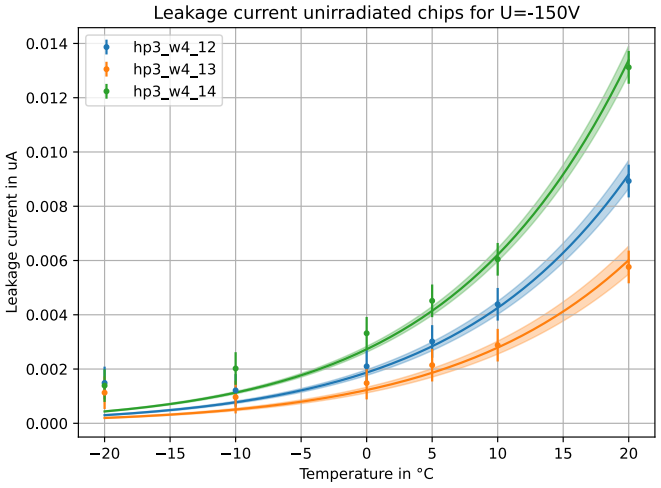

Figure 5.2.: Temperature dependent leakage current for the unirradiated sensors 12,13,14 at $U = -150\,\mathrm{V}$. The filled area displays the 1σ interval of the fit.

5.1.2. Irradiated sensors

As the next step, the irradiated sensors are analyzed. This does not include sensor number 11, which was not irradiated at KAZ but used during one beam test at HIT and is thus analyzed separately from the other sensors. Like with the unirradiated sensors, the leakage current is expected to follow a square root function as in equation 5.1. As this does

not represent the measured data, the leakage current is instead fitted with equation 5.3, taking a linear component into account. The origin of this component is not understood.

$$I = a \cdot \sqrt{-U} - b \cdot U \tag{5.3}$$

The fit of equation 5.3 to the measured leakage current of the irradiated sensors number 6,7,8 and 10 is shown in figure 5.3. The data points have error bars, which are not visible as they are very small with values of $0.034\,\% + 200\,\mathrm{nA}$. The leakage currents are represented well by the fit function. The leakage current after irradiation seems to consist of both an expected square root component and an unexpected linear component. Such a linear component resembles the IV curve of a resistor.

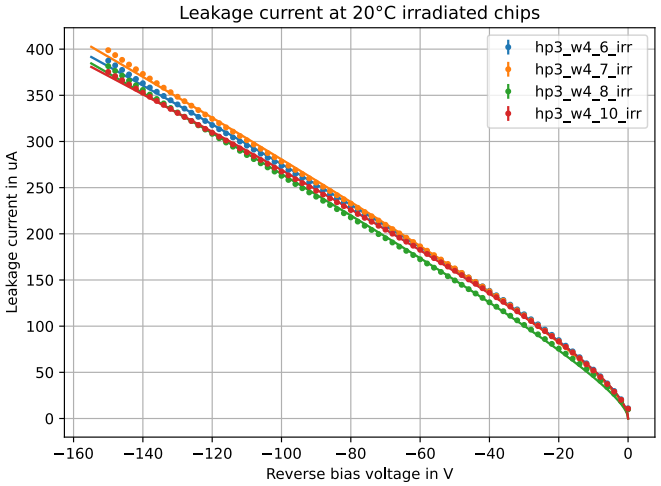

Figure 5.3.: Leakage current of the irradiated sensors 6,7,8,10 as a function of the reverse bias voltage at $T = 20\,^{\circ}\mathrm{C}$

The temperature dependence is not suspected to change due to irradiation and still follows equation 5.2. The corresponding fit is shown in figure 5.4. The fit still resembles the data roughly, however not as well as for the unirradiated sensors, indicating damage not accounted for in the dependency in equation 5.2. The equation can however still be used to roughly estimate the leakage current. The one-sigma interval is not visible as it is very small due to the low measurement uncertainties of $0.034\,\% + 200\,\mathrm{nA}$.

The irradiated sensors show a significantly increased leakage current. Their leakage current is about four orders of magnitude larger than for the unirradiated sensors. In [8], some values for ν from equation 2.2 are provided. These values refer to the parameter after the sensors were heated at $60\,^{\circ}\mathrm{C}$ for 80 min. This was not done here. The values of $\nu \approx 4 \times 10^{-17}\,\mathrm{Acm}^{-}1$ are thus only rough estimates. Previous simulations of the HitPix3 sensor roughly estimated the depletion depth at $d_{\mathrm{irr}} = 40\,\mu\mathrm{m}$ at a bias voltage of $U_{\mathrm{bias}} = 100\,\mathrm{V}$ for irradiated sensors. Neglecting the leakage current of the unirradiated sensors as it is very small, the fluence $\Phi = 1 \times 10^{15}\,\mathrm{cm}^{-2}$ with which the irradiated sensors were irradiated at KAZ, can be used to estimate the leakage current of the irradiated sensors at $U_{\mathrm{bias}} = 100\,\mathrm{V}$. The estimation gives a current of $I_{\mathrm{irr}} \approx 200\,\mu\mathrm{A}$. This is close to the measured currents between $250\,\mu\mathrm{A}$ and $300\,\mu\mathrm{A}$. This means the increased leakage current of the irradiated sensors indicates the expected significant damage to the sensor bulk.

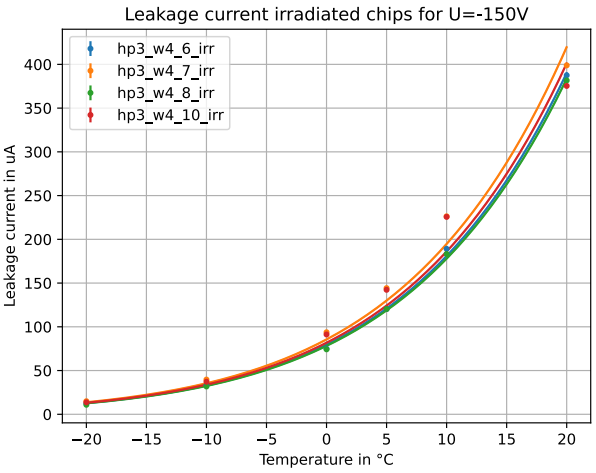

Figure 5.4.: Temperature dependent leakage current of the irradiated sensors 6,7,8,10 at $U = -150\,\mathrm{V}$

5.1.3. Sensor number 11

Initially, the leakage current of sensor number 11 was measured just at room temperature with a measurement uncertainty of $0.031\,\% + 20\,\mathrm{nA}$. This measurement is fitted with the first part of equation 5.3. The fit yielding a parameter $a = (0.0939 \pm 0.0002)\,\mu\mathrm{AV}^{-\frac{1}{2}}$ can be found in figure 5.5. The fit function seems to represent the data, even though the measurement shows a step at around $U = -20\,\mathrm{V}$. This stems from a falsely adjusted power supply. The sensor has since been damaged prohibiting a new measurement.

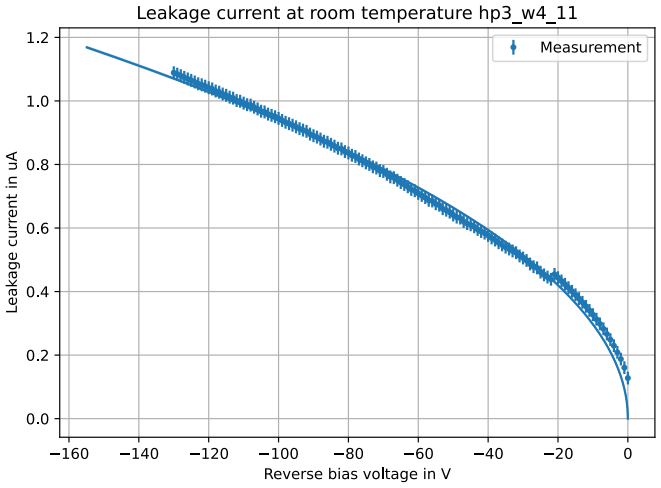

Figure 5.5.: Leakage current sensor number 11 before damages at room temperature

The leakage current of sensor number 11 is now compared to the sensors irradiated at KAZ. The leakage current for sensor number 11 is measured up to bias voltages of $U_{\mathrm{bias}} = -130\,\mathrm{V}$. To avoid damage to the sensors, usually lower voltages are used. A bias voltage of $U_{\mathrm{bias}} = -100\,\mathrm{V}$ is used to compare the leakage currents. This is done via the data from the fits in table A.1. The average leakage current of the unirradiated sensors is $I_{\mathrm{unirr}} = 7.43\,\mathrm{nA}$, of the irradiated sensor it is $I_{\mathrm{irr}} = 272.5\,\mu\mathrm{A}$. Sensor number 11 shows a leakage current of $I_{11} = 0.939\,\mu\mathrm{A}$. Previous simulations roughly estimated the depletion depth at $d_{\mathrm{irr}} = 40\,\mu\mathrm{m}$ for irradiated and $d_{\mathrm{unirr}} = 65\,\mu\mathrm{m}$ for unirradiated sensors. According

to equation 2.2, the fluence Φ_{11} sensor number 11 received can be estimated according to eqaution 5.4. As the leakage current of sensor number 11 is closer to the unirradiated than to the irradiated sensors, its depletion depth is assumed to be that of an unirradiated sensor.

$$\begin{aligned}\Phi_{11} &= \frac{I_{11}}{I_{\text{irr}}}\frac{d_{\text{irr}}}{d_{\text{unirr}}}\Phi_{\text{irr}} \\ &\approx 2.1 \times 10^{-3}\Phi_{\text{irr}}\end{aligned} \tag{5.4}$$

Apparently, sensor number 11 received a fluence roughly 500 times smaller than the sensors irradiated at KAZ. The leakage current of unirradiated sensors is neglected here as it is small compared to the leakage current of sensor number 11. It is however important to note that the dependency in equation 2.2 requires the sensors to be heated to 60 °C for 80 min to reach an annealing state (see [8]), which was not done here. The result is thus only a rough estimate.

During the characterization process in the climatic chamber, sensor number 11 seems to have been damaged. As this has not been observed before, irradiation cannot be the origin of this effect, which is thus not investigated further.

5.1.4. Sensor number 9

Compared to the other irradiated sensors, sensor number 9 shows an increased leakage current. It is investigated further here. During the measurement a compliance current of 500 µA is used to avoid damage to the sensor bulk. As sensor number 9 shows a higher leakage current at room temperature, the sensor is not tested up to a reverse bias voltage of −150 V. The leakage current is shown in figure 5.6 with a fit of equation 5.3 yielding parameters $a = (3.01 \pm 0.04)\,\mu\text{AV}^{-\frac{1}{2}}$ and $b = (5.434 \pm 0.006)\,\frac{\mu\text{A}}{\text{V}}$. Comparing this to the fit parameters of other irradiated sensors in table A.1, the linear component has a significantly higher influence on the leakage current, which indicates larger damaged areas.

The temperature dependence of the leakage current is investigated in figure 5.6, where the data is fitted with equation 5.2 with a parameter of $\kappa = (1.6900 \pm 0.0008) \times 10^6\,\mu\text{A/K}^2$. This is comparable to the values for other irradiated sensors indicating that the sensor, is not damaged similar to sensor number 11. Instead, the increased leakage current seems to be a result of the irradiation. It is however unclear why this sensor appears to be more damaged.

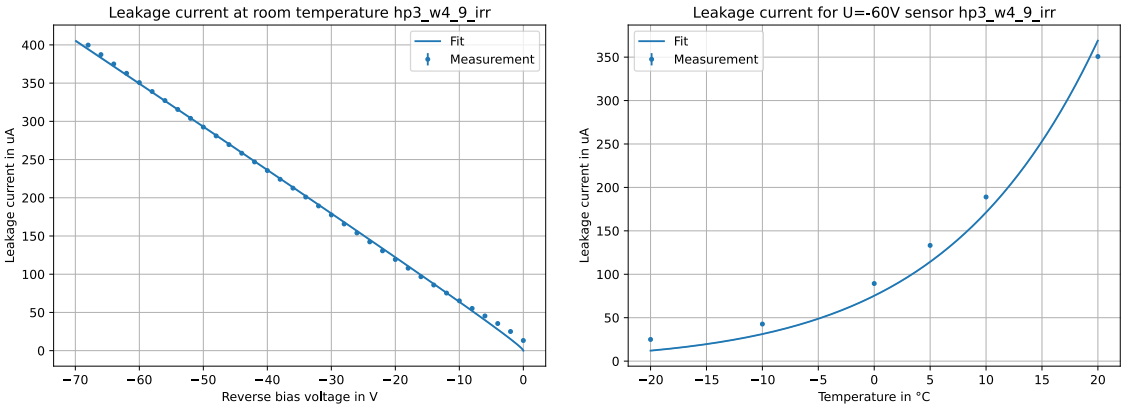

Figure 5.6.: Leakage current as a function of the reverse bias voltage (left) and the temperature (right) for sensor number 9

5.2. Latency scans

The latency scans of sensor number 6 can be found in figure 5.7. As the scans look very similar for all sensors, and show, that the shift register readout is working for all sensors. It is therefore possible to operate the sensors at the full 180 Mbit/s without expecting any issues. As this is also true for the irradiated sensors, the irradiation does not seem to damage the sensor's peripheral electronics.

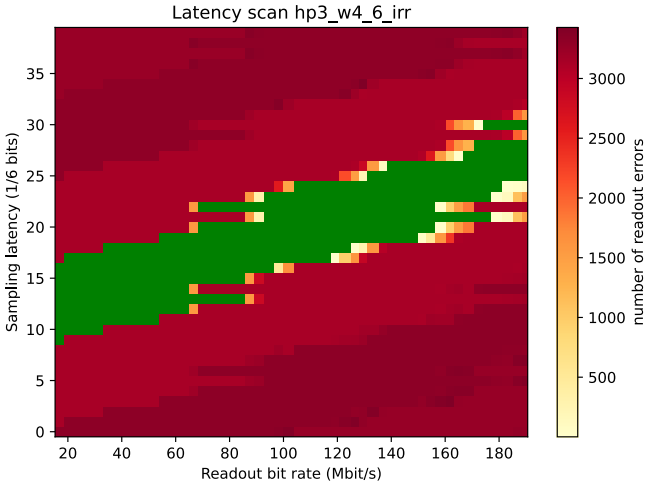

Figure 5.7.: Latency scan for sensor number 6. The different shades of red indicate the number of readout errors while green indicates no readout errors.

5.3. Charge injection measurements

To extract the relevant data from the results of the charge injection measurement, efficiency is calculated for every pixel at every global threshold setting and every charge injection voltage. The efficiency is the number of detections of the injected charge divided by the total number of injections. The efficiency is dependent on the voltage used for the charge injection. As the efficiency is zero for low voltages and one for high voltages with a rapid increase somewhere in between, a sigmoid function is fitted to the efficiencies. An example of this is shown in figure 5.8. This is done to derive a 50 % detection threshold voltage, where the pixel changes from an efficiency of zero to one.

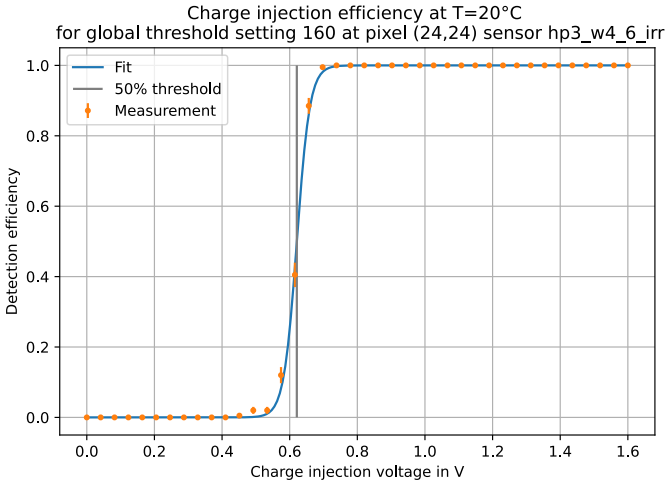

Figure 5.8.: Charge injection detection efficiency as a function of the injection voltage with a sigmoid fit. Example with sensor number 6 and a pixel in the middle of the sensor.

Such a sigmoid fit is done for every pixel of the sensor yielding a 50 % detection threshold voltage for every pixel. An example of this is shown in figure 5.9 with the same conditions as the example of the sigmoid fit.

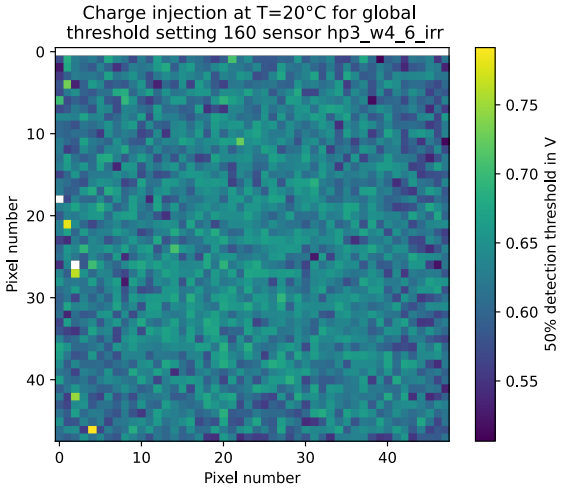

Figure 5.9.: Charge injection 50 % detection threshold voltage for every pixel. Example with sensor number 6

Ideally, all pixels would show the same 50 % detection threshold voltage. This is not observed as there are production imperfections in the pixels leading to a slightly different performance. To compare the calculated 50 % detection threshold voltages for different values of the global threshold setting while considering the spread of the detection threshold voltages, both the average and the corresponding spread need to be obtained. To do so, a histogram is calculated with the frequencies with which a 50 % detection threshold voltage occurs. An example of this distribution for the thresholds shown in figure 5.9 can be seen in figure 5.10. The orange line in the box shows the median of the histogram below. The median corresponds to the second quartile (Q2). The box shows the first and third quartile (Q1 and Q3). The whiskers are the 1.5 times the width of the interquartile range, which is the width of the box. The circles show all remaining data points, named outliers.

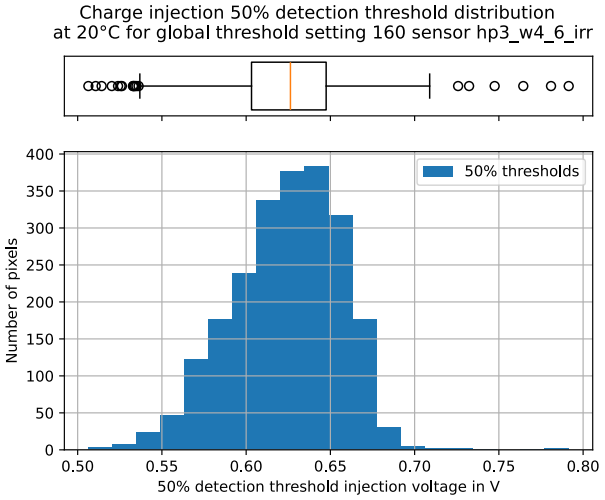

Figure 5.10.: Charge injection 50 % detection threshold voltage distribution. Example with sensor number 6

The relation between the 50 % detection threshold voltage distribution and the global threshold setting for sensor number 6 can be found in figure 5.11 for the highest and the lowest measured temperature. Outliers were not plotted here to increase readability.

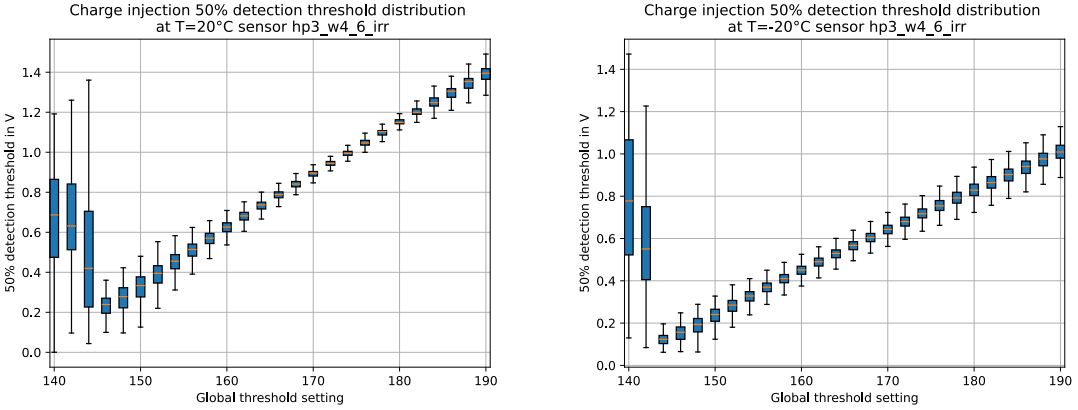

Figure 5.11.: Charge injection 50 % detection threshold voltage distribution depending on the global threshold setting at 20 °C (left) and −20 °C (right). Example with sensor number 6

To be able to compare different sensors, a plot of the median 50 % detection threshold voltages together with the interquartile range is done for all irradiated and unirradiated sensors except the damaged sensor number 9. The result is shown in figure 5.12. Sensor number 11 is listed as an unirradiated sensor here as it was not irradiated at KAZ but only during a beam test. The damaged sensor number 9 is examined in appendix C.

As the plots in figure 5.12 show, there is no significant difference in the behavior of the in-pixel electronics with and without irradiation. It can therefore be concluded that the in-pixel electronics are not affected heavily by the irradiation. For lower global threshold settings, noise is recorded as a signal regardless of the charge injection voltage. It is thus possible that for some pixels noise inhibits the correct identification of the 50 % detection threshold leading to both false 50 % detection thresholds and a large variance across the pixels. All sensors should thus be operated with a high enough global threshold setting to avoid the detection of noise. As it can be read from the plots in figure 5.12, global threshold settings below 150 should be avoided.

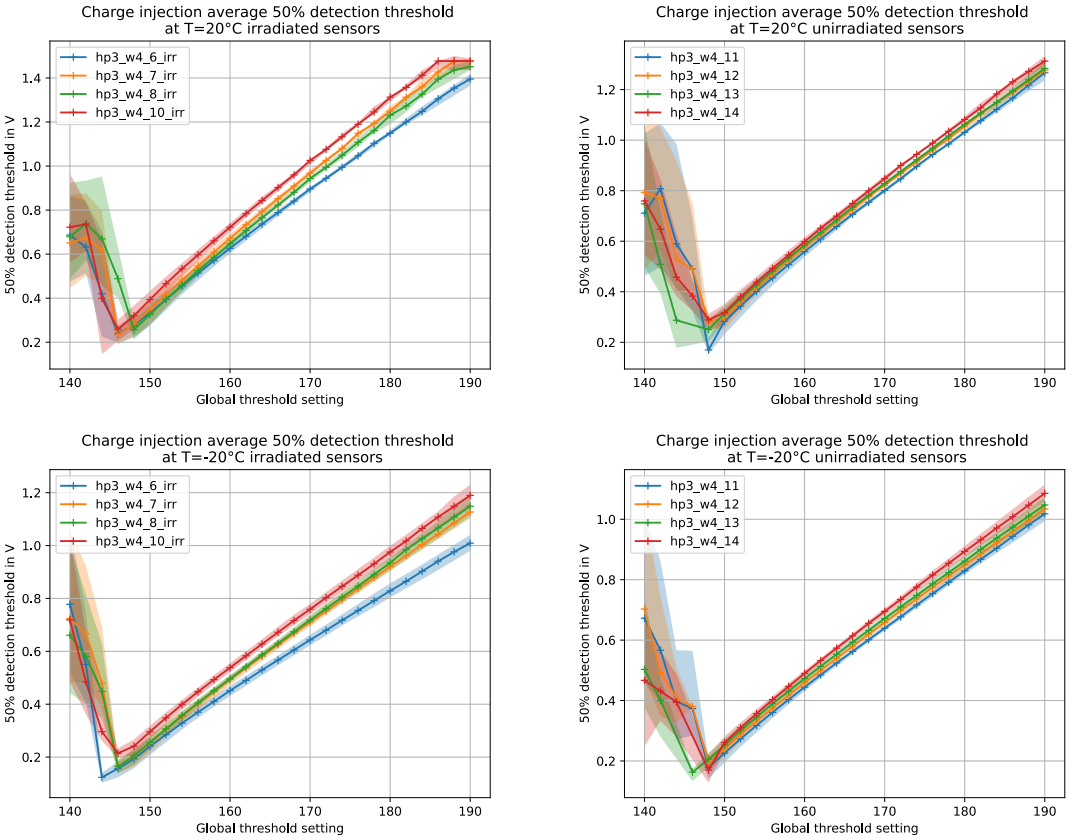

Figure 5.12.: Charge injection median 50 % detection threshold voltage for all sensors. Irradiated (left) and unirradiated (right) sensors at 20 °C (top) and −20 °C (bottom). The filled areas show the area between the Q1 and the Q3 quartile.

In the results in figure 5.12, a slight temperature dependence can be observed. This may need to be considered when choosing the optimal global threshold setting for the beam monitoring with a cooling system to avoid the detection of noise.

5.3.1. Influence of dac-tune optimization on the detection threshold

As mentioned before in section 4.1.3, the dac-tune optimization aims to distribute the 50 % detection thresholds as evenly as possible across the pixels.

One unirradiated and one irradiated sensor were measured with and without dac-tune optimization to verify this. In figure 5.13, the result is shown. Disregarding the noise-disturbed values for low global threshold settings, the median seems mostly unaffected while the interquartile range is much smaller with optimization for both irradiated and unirradiated sensors when regarding global threshold settings between 165 and 185. For lower settings, the 1σ interval increases to values even larger than without optimization. It can thus be considered to adjust the optimization procedure according to the expected global threshold setting that will be used.

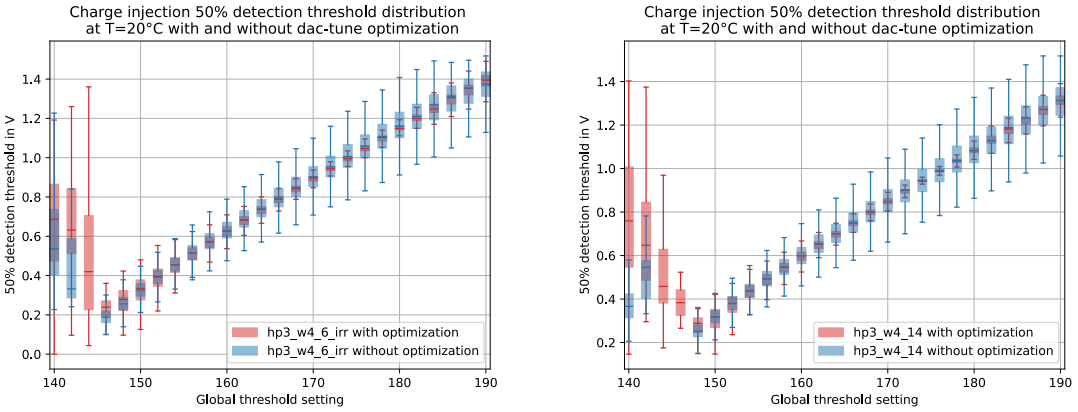

Figure 5.13.: Charge injection 50 % detection threshold voltage distribution as a function of the global threshold setting with and without dac-tune optimization. Irradiated and unirradiated sensors 6 and 14.

5.4. Source profile analysis

In the following, the frame measurements done with the counter readout mode are examined. To classify the ability to locate the Sr-90 source, the profile of the source is analyzed. The profile is characterized by the median hit rate per pixel dependent on the distance from the position of the source. The expected dependence is difficult to estimate as the measurements were not done using an aperture. Instead, the Sr-90 source is encapsulated in a piece of acrylic glass which is open at the bottom. As the opening is just a small hole, particles are passing through differently thick acrylic glass layers before hitting the sensor. The difficult geometric form makes it difficult to calculate a suitable (fit) function to fit the data. This is instead done with a Gaussian curve as it represents the data well. The fit is done to allow for an easier evaluation of the profile. To avoid a noise disturbed result, noisy pixels are masked and not further considered. A pixel is considered noisy if the noise detection rate exceeds 1 % of the detection rate with a Sr-90 source. Depending on the measurement, between 1 % and 15 % of pixels are typically masked.

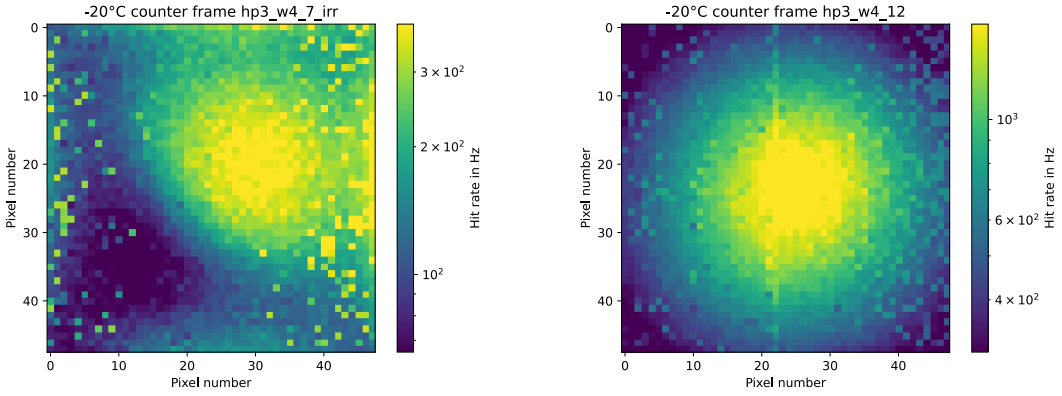

Figure 5.14.: Example of frame measurement with counter readout mode for sensors number 7 and 12 at −20 °C. Measurements with $U_{\text{bias}} = -150\,\text{V}$ and a global threshold setting of 160. Plotted is the measurement with Sr-90 without corrections for noise. The color bar limits are 5 %, meaning that both the 5 % of pixels with the lowest and highest hit rate are all colored blue or yellow.

5.4.1. Comparison between sensors

To analyze the influence of radiation on the performance of the sensors, the source profile is compared for all measured sensors. For $T = -20\,°\mathrm{C}$, this is shown in figure 5.15. The unirradiated sensors show a hit rate one order of magnitude larger than the irradiated sensors. Despite this, the Gaussian shape is visible for most sensors. This means that the position of the source is detectable and while the damage due to radiation has influenced the hit rate substantially, the irradiated sensors can still be used to detect the position of the source.

As sensors number 7 and 12 show the highest hit rates, they will be used in the following to compare other parameters.

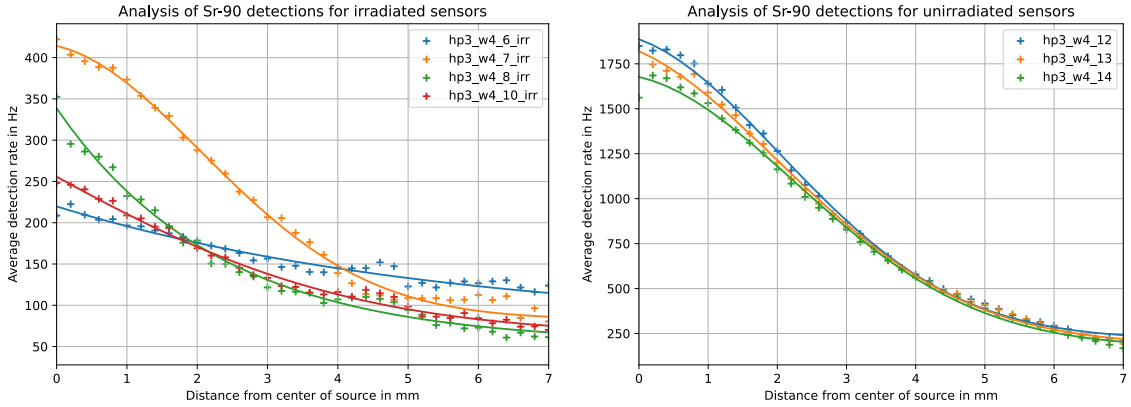

Figure 5.15.: Source profile comparison between sensors. The plots show the average hit rate of pixels of irradiated (left) and unirradiated (right) sensors as a function of distance from the center of the Sr-90 source. The data is fitted with a Gaussian curve. Measurement with $T = -20\,°\mathrm{C}$, $U_{\mathrm{bias}} = -150\,\mathrm{V}$ and a global threshold setting of 160

5.4.2. Temperature dependence

As the goal of this thesis consists of analyzing the performance of the irradiated sensors at different temperatures, the temperature dependence is examined here. Figure 5.16 shows the detected profile of the source for both an irradiated and an unirradiated sensor at different temperatures. While the difference between different temperatures consists mostly of a scaling of the hit rate for the unirradiated sensor, the irradiated sensor is not able to produce well-detectable profiles for $T = 0\,°\mathrm{C}$ and $T = 20\,°\mathrm{C}$. Despite the hit rate being very small at those temperatures, the hit rate increases with distance from the source. As the source is located roughly in the middle of the sensor, the edges seem to produce these increased hit rates. The effect is examined in detail in section 5.7.1. The increased temperature dependence in the ability to locate the source shows that a cooling system can increase the performance of the sensors drastically. It is also apparent that cooling to $T = 0\,°\mathrm{C}$ might not be enough to locate the Sr-90 source reliably. As the beam monitoring system will be used with HIPs and not MIPs such as the beta particles from the Sr-90 source, this might not be true for the operation at the ion beam therapy facility.

5.4.3. Comparison of different settings

The performance of the sensors depends on the settings used during the measurement. To investigate this, a profile analysis is done to compare different values of the reverse bias voltage, the global threshold setting and whether the dac-tune optimization is activated or not. This is done for both irradiated and unirradiated sensors allowing for an evaluation of whether the optimal settings are different for irradiated sensors.

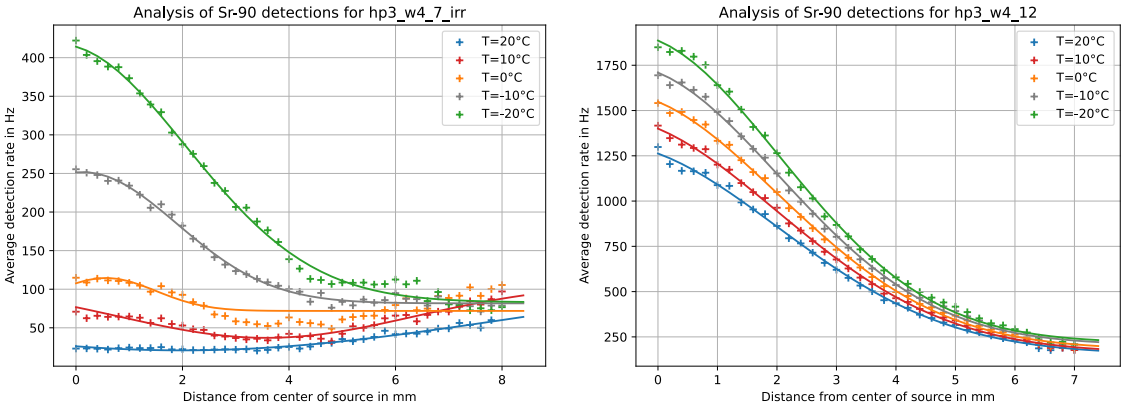

Figure 5.16.: Source profile comparison at different temperatures. The plots show the average hit rate of pixels of one irradiated (left) and one unirradiated (right) sensor as a function of distance from the center of the Sr-90 source. The data is fitted with a Gaussian curve. Measurement with $U_{\text{bias}} = -150\,\text{V}$ and a global threshold setting of 160

5.4.3.1. Reverse bias voltage

To examine the influence of the reverse bias voltage, sensors number 7 and 12 are used to produce profiles of the source for different voltages. This is shown in figure 5.17. Apparently, the hit rate of both sensors increases with the reverse bias voltage. As a higher reverse bias voltage increases the depth of the depletion zone, the volume in which particles are detected increases, leading to a higher detection rate regardless of damage due to radiation. While the position of the source is still detectable even for low reverse bias voltages, it becomes much clearer for higher values. This is true for both irradiated and unirradiated sensors. Regardless of whether the sensor is damaged by irradiation, it should always be operated at the highest reverse bias voltage which does not damage the sensor.

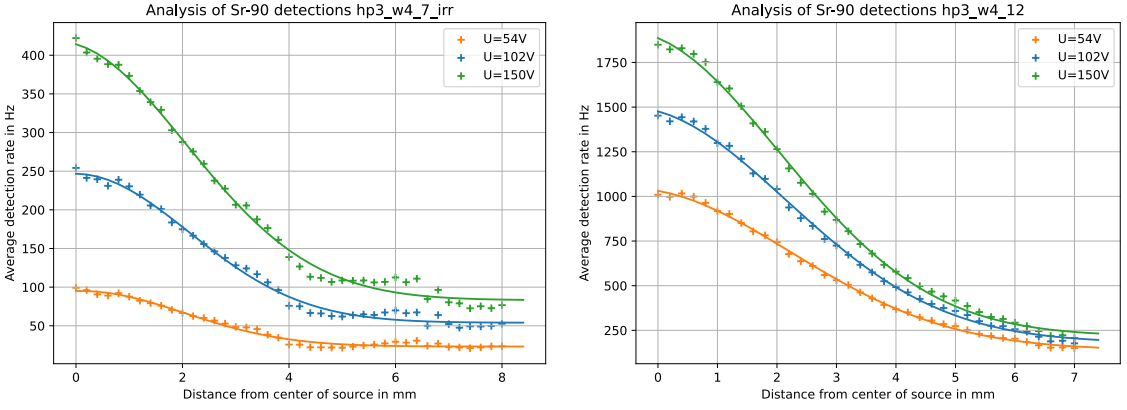

Figure 5.17.: Source profile comparison at different bias voltages. The plots show the average hit rate of pixels of one irradiated (left) and one unirradiated (right) sensor as a function of distance from the center of the Sr-90 source. The data is fitted with a Gaussian curve. Measurement at $T = -20\,^{\circ}\text{C}$ with a global threshold setting of 160

5.4.3.2. Global threshold setting

The influence of the global threshold setting on the profile is to be analyzed. To do so, different profiles are plotted for various global threshold settings. In figure 5.18, the profiles show a decrease in the hit rate with increasing threshold. The profiles for lower thresholds

are not plotted because they are heavily affected by noise. Similarly to the comparison of different reverse bias voltages, all plotted global threshold settings can be used to locate the source. In this case, the global threshold setting should be chosen as low as possible to get maximum hit rates but high enough to avoid noise. For irradiated sensors, this optimal global threshold setting can be higher than for unirradiated sensors because, as previously discussed, the irradiated sensors have a lower hit rate resulting in a larger influence of the same level of noise. Otherwise, the global threshold setting has the same influence on the profile as for unirradiated sensors.

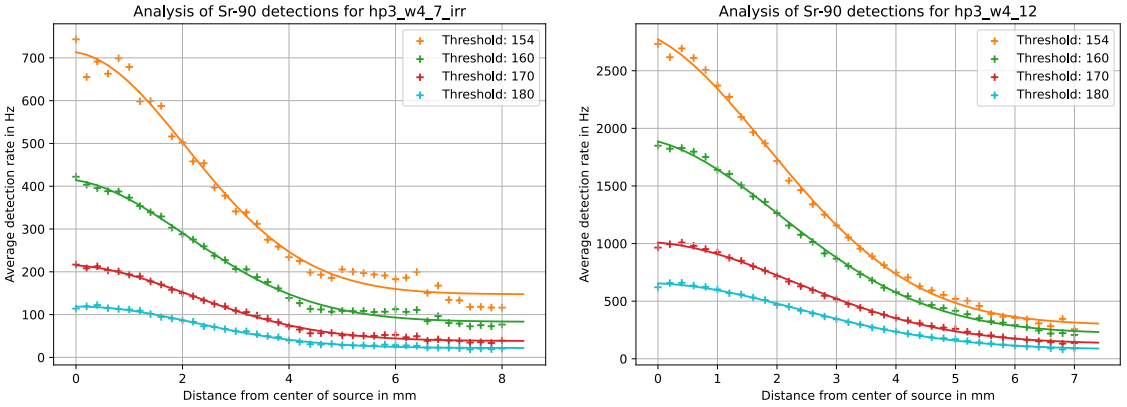

Figure 5.18.: Source profile comparison at different global threshold settings. The plots show the average hit rate of pixels of one irradiated (left) and one unirradiated (right) sensor as a function of distance from the center of the Sr-90 source. The data is fitted with a Gaussian curve. Measurement at $T = -20\,°\mathrm{C}$ and $U_{\mathrm{bias}} = -150\,\mathrm{V}$

5.4.3.3. Dac-tune optimization

As previously discussed, the dac-tune optimization uses charge injection measurements to tune the global threshold setting for each pixel individually to achieve a more consistent actual detection threshold, which is supposed to lead to smoother frame measurements. Most measurements were done with the optimization but for sensors 6 and 14 there are also measurements without the optimization. The differences are shown in figure 5.19. The unirradiated sensor does not show a large difference, which is due to the fact that the profile consists of the median hit rate for pixels with a certain distance from the source. The irradiated sensor shows a completely different result. Near the source, the hit rate is significantly reduced. This indicates an unsuccessful optimization. This is not further investigated in this thesis.

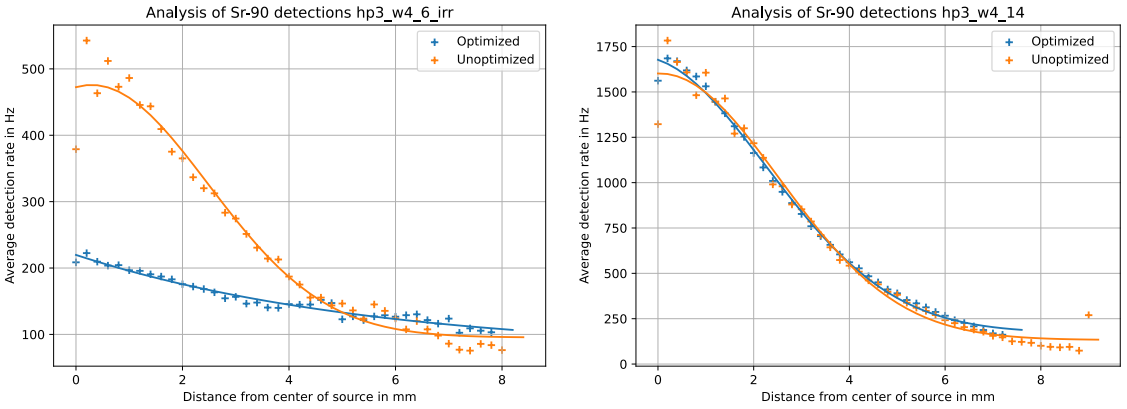

Figure 5.19.: Source profile comparison with and without dac-tune optimization. The plots show the average hit rate of pixels of one irradiated (left) and one unirradiated (right) sensor as a function of distance from the center of the Sr-90 source. The data is fitted with a Gaussian curve. Measurement at $T = -20\,°\mathrm{C}$, $U_{\mathrm{bias}} = -150\,\mathrm{V}$ with a global threshold setting of 160

5.5. Efficiency analysis

To quantify how well an irradiated sensor can detect particles from the Sr-90 source, the hit rates are compared to those of an unirradiated sensor. As all unirradiated sensors show very similar hit rates as displayed in figure 5.15, it does not matter which one is chosen. In the following, this reference sensor is sensor number 12. As the irradiated sensors show artificially high hit rates on the edges, which is discussed in section 5.7.1, the hit rates are compared only in the area of 1 mm from the center of the source. As the position of the sources is not the same for every measurement, the efficiency is calculated as the ratio of the hit rate of every pixel of the irradiated sensor and the calculated hit rate of the unirradiated reference sensor at the same distance from the source. This reference hit rate is calculated by fitting the profile of the source like it is shown in section 5.4 and using it to estimate the hit rate an unirradiated sensor would detect at a pixel with a certain distance from the source. From the efficiencies of the pixels in the area of 1 mm from the center of the source, the median is calculated to estimate the detection efficiency of the sensor.

To avoid false results due to noise, pixels deemed noisy are masked and not further regarded. A pixel is considered noisy if the detection rate without a source exceeds 1 % of the detection rate with a Sr-90 source. Again, depending on the measurement, between 1 % and 15 % of pixels are typically masked.

The efficiency is always calculated for the same operational parameters including the temperature, the global threshold setting and the reverse bias voltage. The efficiency is thus an easy way to estimate how well the sensor is able to perform. It is also calculated for different temperatures in order to evaluate the ideal cooling temperature.

5.5.1. Comparison between sensors

The temperature dependent efficiency for the irradiated sensors 6,7 and 10 is shown in figure 5.20. Sensor number 8 is not included here as the source seems to be located on the very edge of the sensor, making it impossible to exclude detections from the sensitive edge channels, which would lead to falsely high efficiencies. In general, the efficiency decreases with increasing temperature. All sensors show a similar temperature dependence even though the efficiencies differ. As all sensors were treated and measured equally, these deviations must stem from differences in the sensors.

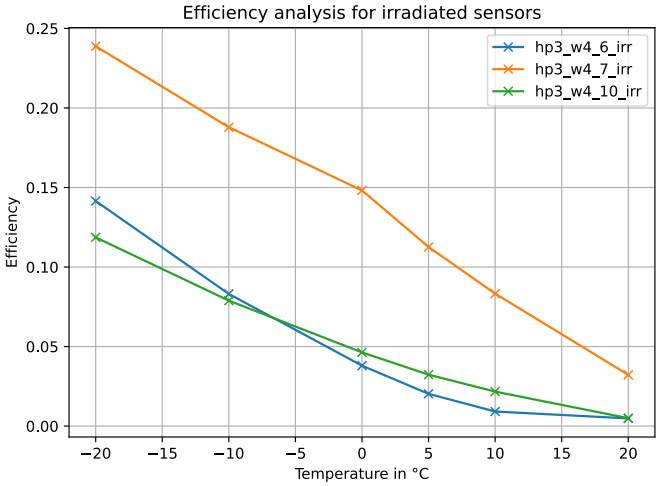

Figure 5.20.: Efficiency comparison between irradiated chips as a function of temperature. Measurement at $U_{\text{bias}} = -150\,\text{V}$ with a global threshold setting of 160. The lines between the data points are simply shown to increase the readability.

5.5.2. Comparison of different settings

Similarly to the source profile analysis 5.4, the efficiency is compared for different settings to determine the ideal operational parameters for the sensors.

5.5.2.1. Reverse bias voltage

The efficiency for different reverse bias voltages in figure 5.21 shows that the total hit rate of the irradiated sensors decreases faster with lower reverse bias voltages than for unirradiated sensors. This is because the reference values are also measured with the lower reverse bias voltages. A reverse bias voltage which is as high as possible thus is all the more important for irradiated sensors.

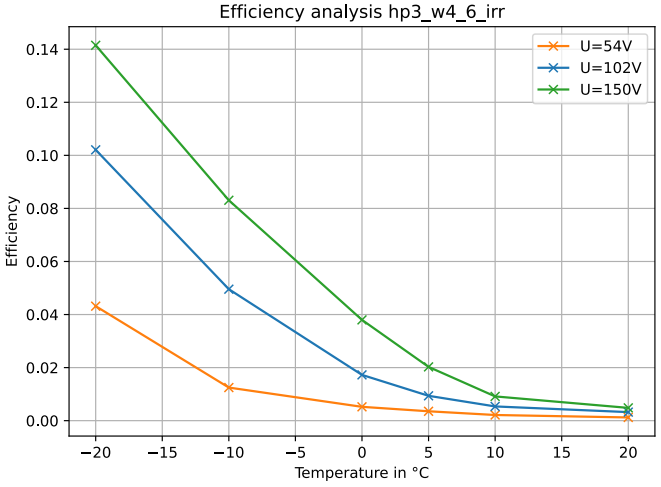

Figure 5.21.: Efficiency of sensor number 6 for different bias voltages as a function of temperature. Measurement with a global threshold setting of 160. The lines between the data points are simply shown to increase the readability.

5.5.2.2. Global threshold setting

The temperature dependent efficiency of sensor number 6 is shown for different global threshold settings in figure 5.22. Similarly to the reverse bias voltage, the global threshold

setting plays an important role, as the efficiency decreases significantly when the global threshold setting is not optimal. A nonoptimal global threshold setting thus has a larger influence on irradiated sensors than on unirradiated ones. As the final ion detection system will not be detecting MIPs, the global threshold setting might not have such a strong influence.

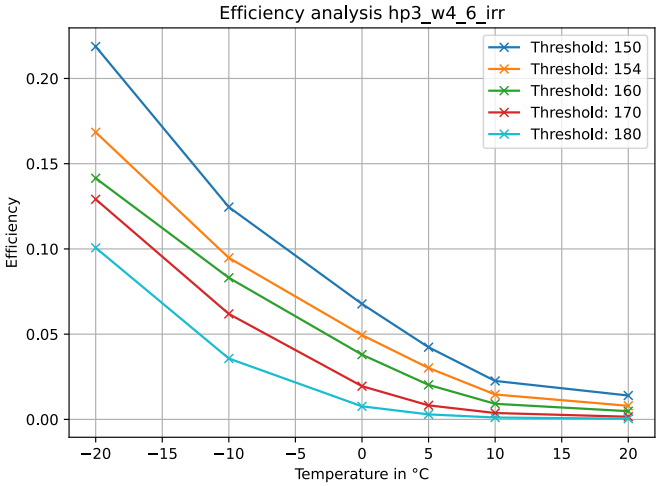

Figure 5.22.: Efficiency of sensor number 6 for different global threshold settings as a function of temperature. Measurement at $U_{\text{bias}} = -150\,\text{V}$. The lines between the data points are simply shown to increase the readability.

5.5.2.3. Dac-tune optimization

As for the source profile analysis, the efficiency is also analyzed without a dac-tune optimization. As it can be seen in figure 5.23, the efficiency is higher without optimization. It is important to note that the dac-tune optimization might influence the average detection threshold. This can influence the detection rate and thus the efficiency. To resolve this issue, the dac-tune optimization should be changed to work well for irradiated sensors as well.

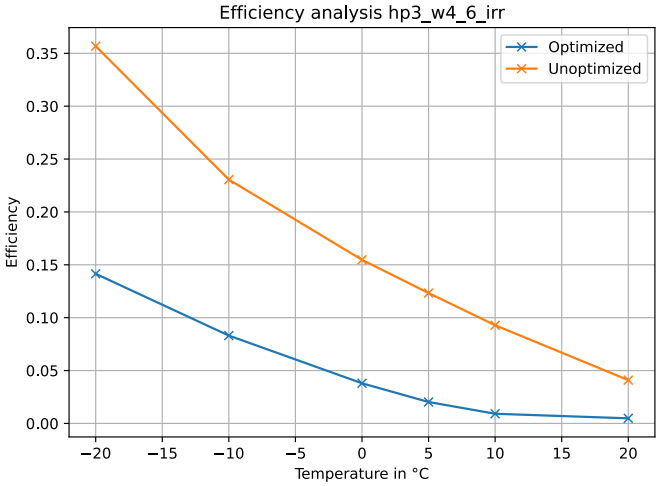

Figure 5.23.: Efficiency of sensor number 6 with and without dac-tune optimization as a function of temperature. Measurement at $U_{\text{bias}} = -150\,\text{V}$ with a global threshold setting of 160. The lines between the data points are simply shown to increase the readability.

5.6. Source profile of the carbon beam

At HIT, beam tests are performed to test the sensors with ions. During one of these beam tests, the carbon beam was measured with both an irradiated and an unirradiated sensor. The profile of the beam is shown in figure 5.24. Compared to profiles of the Sr-90 source in figure 5.15, the beam is visible as a much sharper peak.

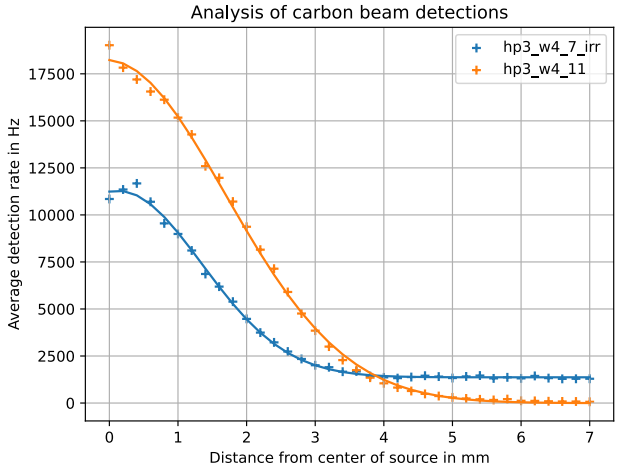

Figure 5.24.: Source profile of the carbon beam for one irradiated and one unirradiated sensor. Measurement of the average detection rate as a function of distance from the center of the source at room temperature, $U_{\text{bias}} = -90\,\text{V}$ and a global threshold setting of 175 for sensor number 11, $U_{\text{bias}} = -50\,\text{V}$ and a global threshold setting of 155 for sensor number 7. Carbon beam with an intensity of $5.0 \times 10^6\,\text{s}^{-1}$ and an energy of $430.10\,\frac{\text{MeV}}{\text{u}}$.

To calculate an efficiency, sensor number 11 is used as a reference. The efficiency is then calculated analogously to section 5.5. This yields an efficiency of 0.61. This is far better than the results obtained from the measurements with the Sr-90 source. It is however important to note that the efficiency here is calculated not for the same reverse bias voltage and global threshold. The reverse bias voltage was chosen to avoid damage to the irradiated sensor, while the global threshold was chosen as low as possible without detecting unusually high noise detection rates. The resulting efficiency can thus not be compared directly to the efficiencies gathered from the measurements with the Sr-90 source. However, the performance of the irradiated sensor at the beam test can still be regarded as much better. This is the case because the signal generated by the HIPs is higher than that generated by MIPs from the Sr-90 source.

5.7. Unexpected events

During the measurements, unexpected results were observed. These are examined in the following.

5.7.1. Sensitive edge channels

During the measurements and first analysis, the irradiated sensors showed unexpectedly high hit rates at the edges. This effect only occurs when a source is present and is thus not pure noise. This presents a significant problem as the edges detect much more hits than in the center where the source is positioned. An example is provided in figure 5.25. With unirradiated sensors, the effect does not occur, see figure D.5. Due to the effect, the adder readout mode can only be used to locate the source if either the edge pixels are masked,

which would drastically reduce the active area, or by changing the dac-tune of the edge pixels in order to receive lower counts. During the characterization process, the sensitive channels also pose a problem because the Sr-90 source should be centered well on top of the sensor for the frame measurements, which is done by viewing a live frame readout and adjusting the position of the source accordingly. As the edge problem is especially strong at high temperatures and the positioning has to be done with the climatic chamber open, the process is very difficult. This results in the source not being positioned centrally during some of the frame measurements on the irradiated sensors.

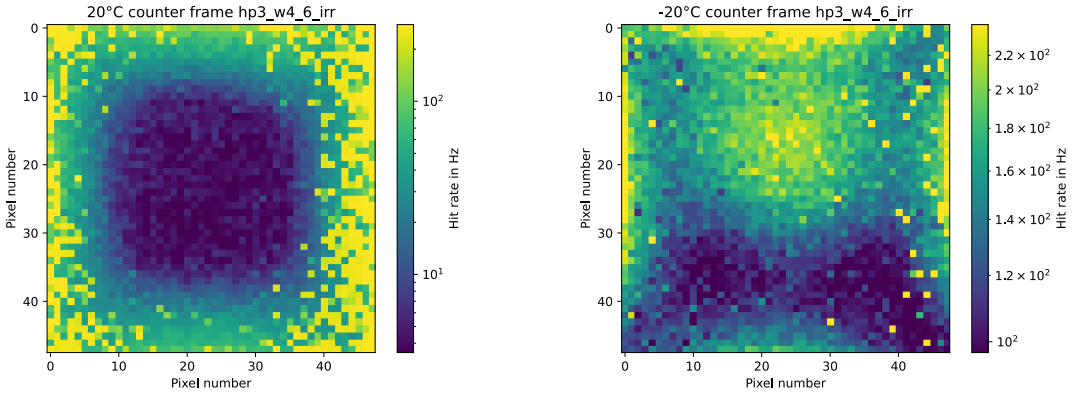

Figure 5.25.: Sensitive edge channels with sensor number 6. Frame measurements for sensor number 6 at $T = 20\,°\mathrm{C}$ and $T = -20\,°\mathrm{C}$ with $U_{\mathrm{bias}} = -150\,\mathrm{V}$ and a global threshold setting of 160. Plotted is the measurement with Sr-90 without corrections for noise at $20\,°\mathrm{C}$ (left) and $-20\,°\mathrm{C}$ (right). It is the average hit rate from 3000 frames with a frame length of 5 ms. The color bar limits are 5 % meaning both the 5 % of pixels with the lowest and highest hit rate are all colored blue or yellow.

5.7.2. Movement of sources

During multiple measurements, where the position of the source is clearly visible in the frame measurements with counter readouts, the position of the source seems to change. This was first discovered during the temperature dependent full characterization of sensor number 11 and was observed again during the measurement of sensor number 14 without dac-tune optimization. In figure D.5 in the appendix, the frame measurements in counter readout mode are plotted. As it is unlikely that the sensor malfunctions in such a way that the position of the source seems to be changed, it has to be assumed that the source actually moved. This is possible, as the climatic chamber can produce vibrations. It is however not certain that this is the cause of the issue. During the measurement, this movement was not apparent, when removing the source. This is however not unexpected as the total movement of the source during the measurements is around 3 mm. This can easily be overlooked but should be looked for in future measurements.

5.8. Basic functionality of the irradiated sensors

In this section, sensors are examined regarding their ability to be used to detect particles from the Sr-90 source. This is ensured if the in-pixel electronics are working as well as the peripheral readout electronics. It is also necessary that the leakage current allows the sensor to be operated at sufficiently high reverse bias voltages to ensure optimal results. It does however not include how well the sensor is able to locate the source or if it needs to be operated at certain conditions like low temperatures.

The examination of the peripheral electronics in section 5.2 and of the in-pixel electronics in section 5.3 did not show any defects to the irradiated sensors compared to the unirradiated

ones. It can thus be assumed that radiation creates only damage to the diode and not to the other components. The analysis of the leakage current shows this radiation damage. Except for sensor number 9, which is suspected to be damaged differently, the sensors do not seem to reach the breakdown voltage and can thus be operated at the desired high voltage. Doing so, the frame measurements showed that the sensors are detecting particles. This means the basic functionality of the irradiated sensors number 6,7,8 and 10 is ensured. Sensors 9 and 11 seem to have been damaged during the measurement process, inhibiting them from working properly. For future measurements, the maximal reverse bias voltage should thus be reduced.

5.9. Ideal operating temperature for the detector

The otherwise undamaged irradiated sensors proved to work in principle. This does however not automatically mean they can be used to detect the beam. As previously explained, the ion beam is substituted with a Sr-90 source. If a sensor can be used to locate the source, it is assumed to be able to detect the ion beam as well. Evaluating the ideal operational temperature for the sensors was done for the Sr-90 source as this ensures the required temperature for the ion beam as well. Possibly the actual temperature for the final detector can be higher but it would work at least as well with lower temperatures.

The required cooling temperature will be evaluated based on the source profile and the efficiency analysis. As seen in figure 5.16, cooling the sensor below $T = 0\,°\mathrm{C}$ allows for a well-recognizable profile, which cannot be said for higher temperatures. As this is heavily influenced by the sensitive edge channels, it is possible to operate the sensor at higher temperatures when either the edge channels are masked or the dac-tune optimization is changed for irradiated sensors to accommodate this problem. As of now, a recognizable profile of the Sr-90 source can only be expected below $T = 0\,°\mathrm{C}$.

The analysis of the efficiency shows a similar result, with efficiencies below $5\,\%$ for temperatures above $T = 0\,°\mathrm{C}$. A low efficiency can however still allow for a detection of the beam and would allow for a much simpler cooling system. It also has to be considered that the beam monitoring system needs to operate at high speeds. Thus the frame length has to be very short. When the efficiency is too low, the total hit count per frame might be too low to locate the beam accurately. As the therapeutic ion beam operates with low intensities in some cases, a low cooling temperature is advantageous.

6. Conclusion

In this thesis, the HitPix3 sensor was introduced as the basic particle detection element of a new monitoring system for ion beam therapy done in facilities such as HIT. HitPix3 is a MAPS built in a HV-CMOS fabrication process. To examine the impact of radiation on the sensors, some sensors were irradiated at a cyclotron with a dose similar to the dose that sensors at the ion beam therapy facility would receive during one year of operation. The irradiated sensors were then tested along with several unirradiated sensors in order to compare the results. As one objective of this thesis was to gather data on the optimal cooling temperature of the monitoring system, the measurements were conducted at different temperatures between 20 °C and −20 °C. The measurements include the leakage current to examine damage to the sensor bulk, latency scans and charge injection measurements concerning the on-sensor electronics and frame measurements to determine the ability of the sensors to detect MIPs from a Sr-90 source.

The unirradiated sensor's leakage current seems to follow theoretical prediction both in its dependence on temperature and reverse bias voltage. For irradiated sensors this is only true regarding the temperature dependence. The expected square root shape of the reverse bias voltage dependent leakage current was not observed. Instead, an additional linear component was seen. Such a linear component can typically be found with resistors. This indicates damage to parts of the sensor which are not accounted for in the theoretical prediction of the bulk current. To test the data transfer from the sensor, latency scans were performed. They show no difference between irradiated and unirradiated sensors, indicating that this is not affected by radiation. For validating the in-pixel electronics, charge injection measurements did not show significant differences between the irradiated and unirradiated sensors. Regarding the frame measurements, only the counter readout mode was used as it offers detailed information about the hit rates for all pixels. The hit rates recorded with irradiated sensors were very low, especially at high temperatures. This makes the detection of the position of the beam more difficult. It was also apparent that the selection of the optimal operational parameters has a greater influence on the detection capabilities of irradiated sensors than for unirradiated ones. The pixels on the edges of the irradiated sensors were observed to show an increased sensitivity making it more difficult to detect the position of the source. This might however be solved by an appropriate dac-tune optimization strategy, which should be investigated in further studies.

During the measurement campaign, two sensors (number 9 and 11) were found to be damaged, presumably due to high reverse bias voltages of up to 150 V. To avoid this in future measurements, this should be reduced to values like 130 V.

Combining the results, it was shown that the HitPix3 sensors are still functioning after irradiation. The performance was observed to increase with lower temperatures. From the data gathered in this thesis, the sensor works best, when being cooled to a temperature as low as possible. As only temperatures up to −20 °C were examined, it is possible that this trend stops somewhere below that. It has however also been observed that the performance

of the irradiated sensors is decreased less compared to the unirradiated ones when using them with HIPs and not MIPs. As cooling to very low temperatures below $-20\,^{\circ}\mathrm{C}$ poses a significant challenge, it needs to be evaluated in the future, if this is necessary for accurately detecting ions. To do that, first, the issue of the sensitive edge channels needs to be resolved by an improved dac-tune optimization. Then, an experimental cooling system can be developed, which allows the cooling of the sensor during testing in the ion beam. For further measurements with the Sr-90 source, a positioning device needs to be constructed to avoid movements of the source.

Appendix

A. Leakage current fit parameters

Table A.1.: Leakage current fit parameters. Parameters of the fit functions 5.3 and 5.2.

Sensor	a in $\mu A V^{-\frac{1}{2}}$	b in $\frac{\mu A}{V}$	κ in $\mu A/K^2$
hp3_w4_6_irr	(11.59 ± 0.02)	(1.596 ± 0.002)	$(1.7905 \pm 0.0008) \times 10^6$
hp3_w4_7_irr	(10.57 ± 0.02)	(1.749 ± 0.002)	$(1.9267 \pm 0.0008) \times 10^6$
hp3_w4_8_irr	(8.44 ± 0.02)	(1.804 ± 0.002)	$(1.7606 \pm 0.0008) \times 10^6$
hp3_w4_10_irr	(11.86 ± 0.02)	(1.505 ± 0.002)	$(1.8413 \pm 0.0008) \times 10^6$
hp3_w4_11	(0.0939 ± 0.0002)	-	-
hp3_w4_12	$(6.68 \pm 0.08) \times 10^{-4}$	-	(42.1 ± 2.4)
hp3_w4_13	$(4.69 \pm 0.08) \times 10^{-4}$	-	(27.6 ± 2.4)
hp3_w4_14	$(1.093 \pm 0.080) \times 10^{-3}$	-	(61.4 ± 2.4)

B. Remaining latency scans

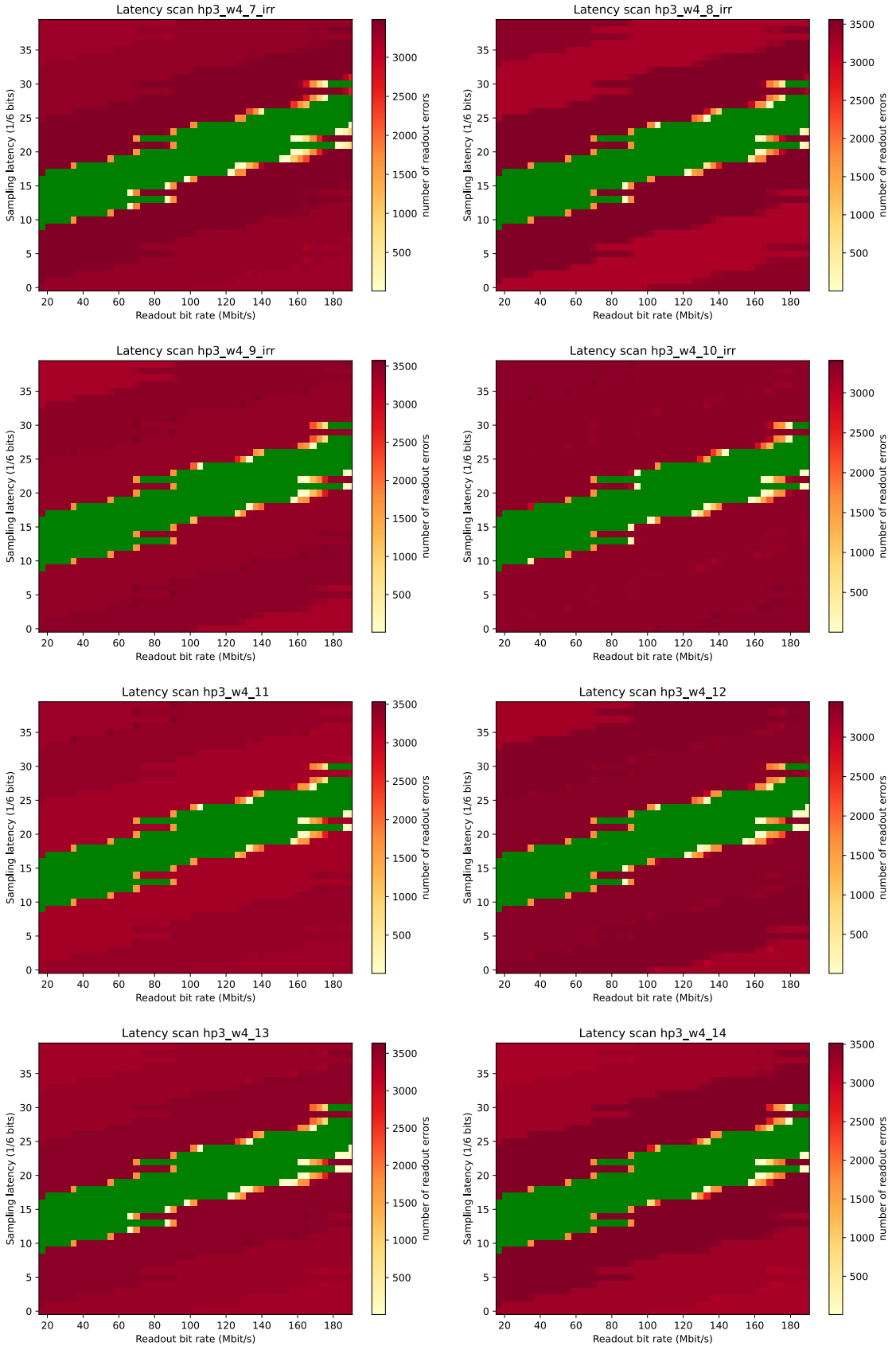

Figure B.1.: Latency scans of the remaining sensors. The different shades of red indicate the number of readout errors while green indicates no readout errors.

C. Charge injection measurement sensor number 9

Sensor number 9 was initially measured at room temperature with the results shown in figure C.2. As it can be seen, the measurement is comparable to other irradiated sensors. The measurement in the climatic chamber shows damage to the sensor which does not stem from irradiation as the sensor was not irradiated between the two measurements. The damaged sensors do not detect any charge injections on about half of the pixels (see figure C.3 and C.4) and the 50 % detection threshold voltage seems to be constant for different global threshold settings (see figure C.3). As this damage does not stem from irradiation, it is not investigated further.

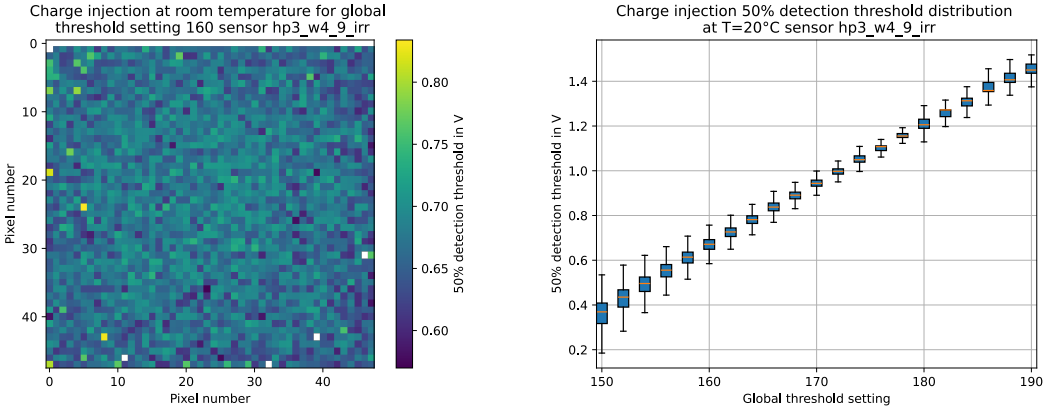

Figure C.2.: Charge injection 50 % detection threshold voltage sensor 9 before damage for every pixel (left) and for different global threshold settings (right).

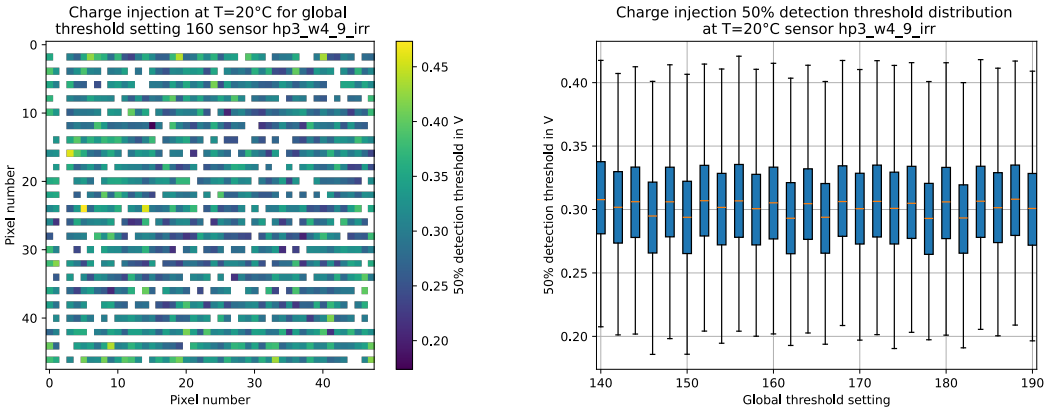

Figure C.3.: Charge injection 50 % detection threshold voltage sensor 9 after damage for every pixel (left) and for different global threshold settings (right).

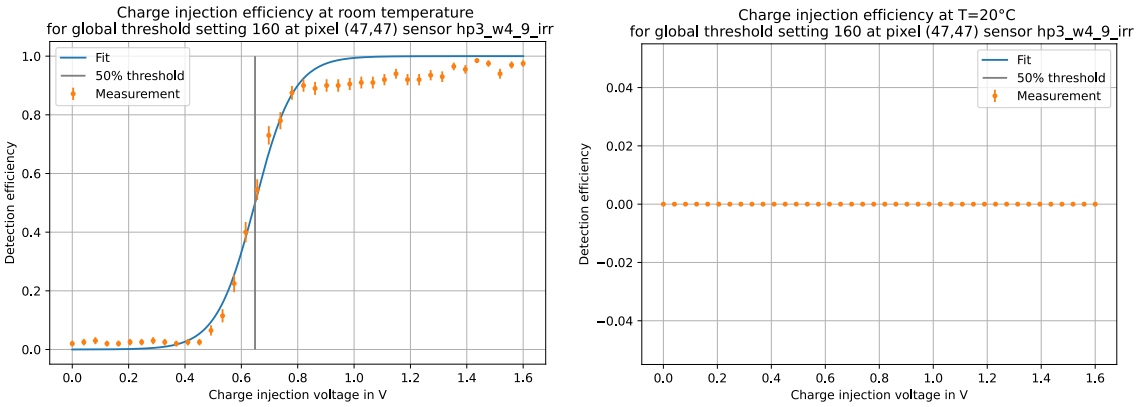

Figure C.4.: Charge injection detection efficiency with sigmoid fit sensor 9. Example with pixel (47,47) before (left) and after (right) damage.

D. Movement of sources

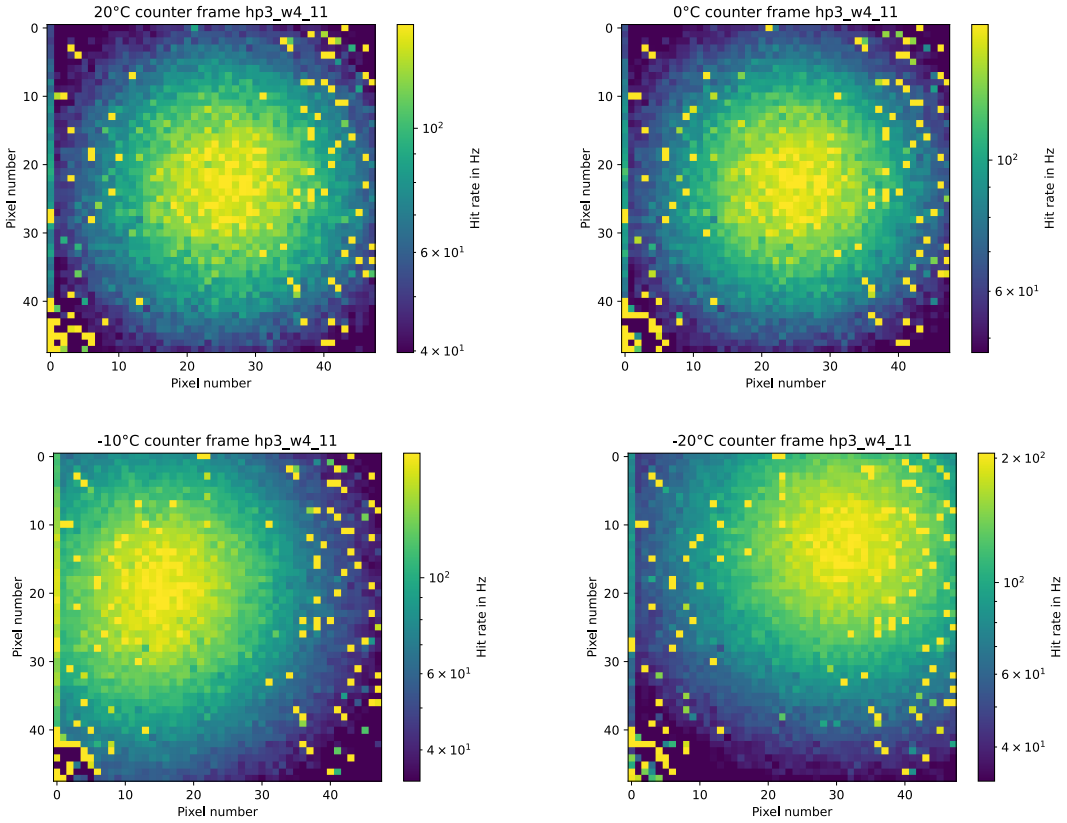

Figure D.5.: Movement of the source with sensor 11. Top: nominal position of the source for all temperatures except $-10\,°C$ and $-20\,°C$, bottom: changed position of the source for the lowest two temperatures. All measurements with $U_{\text{bias}} = -150\,V$ and a global threshold setting of 160. Plotted is the measurement with a Sr-90 source without corrections for noise. It is the average hit rate from 3000 frames with a frame length of 5 ms. The color bar limits are 5 % meaning both the 5 % of pixels with the lowest and highest hit rate are all colored blue or yellow.

Bibliography

[1] T.J. Royce and J.A. Efstathiou, *Proton therapy for prostate cancer: A review of the rationale, evidence, and current state*, *Urologic Oncology: Seminars and Original Investigations* **37** (2019) 628.

[2] A. Brown and H. Suit, *The centenary of the discovery of the Bragg peak*, *Radiotherapy and Oncology* **73** (2004) 265.

[3] O. Jäkel, G. Kraft and C.P. Karger, *The history of ion beam therapy in Germany*, *Zeitschrift für Medizinische Physik* **32** (2022) 6.

[4] S.E. Combs, O. Jäkel, T. Haberer and J. Debus, *Particle therapy at the Heidelberg Ion Therapy Center (HIT) – integrated research-driven university-hospital-based radiation oncology service in Heidelberg, Germany*, *Radiotherapy and Oncology* **95** (2010) 41.

[5] *Heidelberger Ionenstrahl Therapiezentrum*, . `https://www.klinikum.uni-heidelberg.de/fileadmin/hit/dokumente/%HIT_Broschuere.pdf` [Accessed: 02.04.2024].

[6] A. Dierlamm, M. Balzer, F. Ehrler, U. Husemann, R. Koppenhöfer, I. Perić et al., *A beam monitor for ion beam therapy based on HV-CMOS pixel detectors*, *Instruments* **7** (2023) .

[7] W.G. Shin, S.W. Ko, H.J. Song, Y.C. Ju, H.M. Hwang and G.H. Kang, *Origin of bypass diode fault in c-Si photovoltaic modules: Leakage current under high surrounding temperature*, *Energies* **11** (2018) .

[8] M. Moll, *Radiation damage in silicon particle detectors: Microscopic defects and macroscopic properties*, Ph.D. thesis, Hamburg U., 1999.

[9] A. Chilingarov, *Temperature dependence of the current generated in Si bulk*, *Journal of Instrumentation* **8** (2013) P10003.

[10] P.D. Group, R.L. Workman, V.D. Burkert, V. Crede, E. Klempt, U. Thoma et al., *Review of Particle Physics*, *Progress of Theoretical and Experimental Physics* **2022** (2022) 083C01.

[11] *Zyklotron AG*, . `https://www.zyklotron-ag.de/ueber-uns/` [Accessed: 22.04.2024].